Research article

Numerical analysis of biothermal-fluids and cardiac thermal pulse of abdominal aortic aneurysm

EYK Ng* and Leonard Jun Cong Looi

School of Mechanical and Aerospace Engineering, College of Engineering, Nanyang Technological University, 50 Nanyang Avenue, Singapore 639798

* Correspondence: Email: mykng@ntu.edu.sg; Tel: +656790-4455.

Abstract: Abdominal aortic aneurysms are serious and difficult to detect, conditions can be deadly if they rupture. In this study, the heat transfer and flow physics of Abdominal Aortic Aneurysm (AAA) were discussed and associated with cardiac cycle to illustrate the cardiac thermal pulse (CTP) of AAA. A CTP and infrared thermography (IRT) evaluation-based on AAA and abdomen skin surface detection method was proposed, respectively. Infrared thermography (IRT) is a promising imaging technique that may detect AAA quicker and cheaper than other imaging techniques (as biomarker). From CFD rigid-wall and FSI Analysis, the transient bioheat transfer effect resulted in a distinct thermal signature (circular thermal elevation) on the temperature profile of midriff skin surface, at both regular body temperature and supine position, under normal clinical temperature. However, it is important to note that thermography is not a perfect technology, and it does have some limitations, such as lack of clinical trials. There is still work to be done to improve this imaging technique and make it a more viable and accurate method for detecting abdominal aortic aneurysms. However, thermography is currently one of the most convenient technologies in this field, and it has the potential to detect abdominal aortic aneurysms earlier than other techniques. CTP, on the other hand, was used to examine the thermal physics of AAA. In CFD rigid-wall Analysis, AAA had a CTP that only responded to systolic phase at regular body temperature. In contrast, a healthy abdominal aorta displayed a CTP that responded to the full cardiac cycle, including diastolic phase at all simulated cases. Besides, the findings from FSI Analysis suggest the influence of numerical simulation techniques on the prediction of thermal physics behaviours of AAA and abdominal skin surface. Lastly, this study correlated the relationship between natural convective heat transfer coefficient with AAA and provided reference for potential clinical diagnostic using IRT in clinical implications.

Keywords: unsteady blood flow; transient bioheat transfer; cardiac thermal pulse; abdominal aortic aneurysm; abdominal aorta wall; midriff skin surface; isotherms; FSI; CFD rigid-wall

Nomenclature: AAA: Abdominal Aortic Aneurysm; A: Early Systole; B: Peak Systole; C: End Systole; CTP: Cardiac Thermal Pulse; CFD: Computational Fluid Dynamic; D: Peak Diastole; E: End Diastole; FSI: Fluid Structure Interaction; IRT: Infrared Thermography; SEF: Strain Energy Function

Variables: c_p: Specific Capacity, J/(kgK); C_1: Mooney-Rivlin constant 1, kPa; C_2: Mooney-Rivlin constant 2, kPa; d: Material Incompressibility Parameter, Pa^{-1}; $\ddot{d}_s$: Local Acceleration, m/s^2; f_s^B: Body Force per Unit Volume; h: Volumetric Blood Perfusion Rate, 1/(sm^3); h_c: Convective Heat Transfer Coefficient, W/m^{2}K; I_1, I_2: First and Second Invariant of the Cauchy-Green Deformation Tensor; J: Volume Ratio (Deformed Volume over Undeformed Volume); k_t: Thermal Conductivity, W/(mK); p: Pressure, Pa; Q_m: Volumetric Metabolic Rate, W/m^3; T_a: Local Surrounding Air Temperature, K; T_{in}: Initial Blood Inflow Temperature, K; $T_{s,m}$: Average Surface Integral Mean Skin Temperature, K; t: Thickness, m; u: Fluid Velocity Vector; u_g: Moving Coordinate Velocity; V: Volume, m^3

Greek letters: μ: Dynamic Viscosity, Pa·s; ρ: Density, kg/m^3; v: Poisson Ratio; τ_s: Solid Stress Tensor; Ψ_{iso}: Strain Energy Density, J/m^3

Subscripts: b: blood; t: abdominal tissue

1. Introduction

1.1. Background information

Abdominal Aortic Aneurysm (AAA) is a location where the weakened arterial wall becomes blood-filled and dilated. AAA diagnoses are incidental as they are asymptomatic and when they rupture, the condition becomes fatal [1–3]. Thus, early diagnosis and treatment are very important to prevent further complications and even death. 70% of patient who received timely treatment are expected to survive for another 5 years [4].

Diagnosing an aortic aneurysm is not easy. Generally, the common AAA screening procedures are Duplex Ultrasound (DUS), Computed Tomography Angiography (CTA) and Magnetic Resonance Angiography (MRA) [5]. However, these tests except DUS, are cumbersome and may expose patients to radiation during the procedure. Moreover, these procedures require the use of expensive machines which are not commonly found in clinics. Therefore, the lack of required machines in most clinics may indirectly delay diagnoses of most AAAs [6]. On the other hand, late diagnoses lead to higher rupture rate due to progressively dilating AAA [7]. It is estimated that there are 1 million people who have undiagnosed abdominal aortic aneurysms in the United States alone [8]. Although there are some risk factors for developing AAA, including age and family history of the disease [9,10], but there are no current guidelines or good tests to diagnose AAA. Consequently, it results in the high mortality rate of 80% [11].

As such, it will be helpful to promote a less invasive and affordable diagnostic tool, Infrared Thermography (IRT) as an effective as a complimentary tool to detect AAA and reduce mortality rates from the condition.

Till date, the AAA rupture has been studied comprehensively, however, the whole bioheat transfer mechanism of AAA remains unknown. Most literature drew correlations with factors like hypertension, age, gender and smoking [9,10] to the wall stress. In conditions where wall stress exceeds the ultimate strength of arterial wall, they may result in AAA rupture. However, studies correlating the risk of AAA rupture to the external environment temperature are uncommon [12]. Thus,

it is suggestive to note that there is limited research on the bioheat transfer effect of transient blood flow on AAA wall and midriff skin surface currently.

Saxena, Ng, Manchanda et al. [13] correlated the phase shift found in the Cardiac Thermal Pulse (CTP) of the neck skin surface to the severity of stenosis of carotid artery. CTP is defined as localised temperature fluctuations resulted from periodic physiological artery blood flow [13]. As such, this motivated the study of bioheat transfer effect of transient blood flow on AAA wall to find the correlation between CTP and the presence of aneurysm.

In a similar pattern, Ng and Pang [14] proposed IRT to be a less invasive, cost-effective and contactless clinical procedure to identify AAA via thermal elevation on the midriff skin surface [14]. However, the Computational Fluid Dynamic (CFD) analysis adopted was not a realistic approach as it assumed an overall skin convective heat transfer coefficient, h_c and neglected the interaction between the fluid and structure of the dynamic blood flow and anisotropic AAA wall motion. To simulate the real clinical setting where patient is in supine position, realistic abdomen's h_c should be used.

In addition, flexible vascular walls tend to deform as a result of hemodynamic forces which may alter the blood flow path, and thus affecting the fluid dynamic [15,16]. In other terms, the material properties of the aneurysm wall influence the blood flow behaviour [17]. Generally, the AAA is assumed as a large elastic artery [18,19]. Holzapfel and Ogden [20] review on the biomechanics and mechanobiology of arterial walls emphasizes the highly non-linear and incompressible continuum biomechanics. The non-linear nature effectively accounts the large dilations in aneurysms [16]. Therefore, studying AAA constitutes a FSI problem when accounting for the geometrical changes of solid structure. Moreover, the modelling techniques such as Computational Solid Stress (CSS), CFD and Fluid-Structure Interaction (FSI) influence the estimation of AAA behaviour [17,21]. Hence, to increase accuracy of overall AAA behaviour findings, studies link the fluid dynamics component with the solid domain component of the simulation [15,17,22–24]. To date, several studies have described the dynamic nature of arterial wall using various mathematical model [16,25–28]. In view of all that has been mentioned so far, one may suppose that Mooney-Rivlin model developed by Raghavan and Vorp [29] is relatively relevant, accurate and reputable AAA model.

1.2. Objective

The study serves to
1) introduce the relationship between CTP and the presence of AAA using CFD and FSI Analysis. Hypothesis 1: The outcome of CFD rigid-wall Analysis was hypothesised that AAA has larger phase shift in comparison with healthy abdominal aorta model due to the recirculation of blood flow at AAA bulge. However, due to the deformable property of AAA wall in FSI study, the blood flow physics might be drastically affected and hence CTP was hypothesised to be absent.
2) investigate the impact of reduced natural convective heat transfer coefficient, h_c, resulted from supine position during clinical diagnostic process on the temperature (isotherm) contour of midriff skin surface introduced in Ng and Pang [14] using CFD rigid-wall and FSI Analysis. Hypothesis 2: At lower h_c, the midriff skin surface was hypothesised to have a warmer temperature contour due to the lower heat transfer rate.
3) determine the effect of numerical techniques in studying the transient bioheat transfer effect of AAA and thermal signature on midriff skin surface. Hypothesis 3: Comparing the results from CFD rigid-wall Analysis, the temperature contour on midriff skin surface in FSI Analysis was hypothesised to be similar to certain extent, as the same abdominal tissue model property was utilised.

Table 1. Studies that have commented on the bioheat transfer effect of transient blood flow on aorta wall and skin surface.

Author	Study Design	Significant Findings
Saxena, Ng, Manchanda et al. [13]	CTP at the neck skin surface as a measure of stenosis in the carotid artery	Successive phase shift resulted by CTP with the increase in *stenosis in the carotid artery*
Ng and Pang [14]	Thermal elevation on midriff skin surface as a potential diagnostic feature for Abdominal Aortic Aneurysm (rigid-wall) using Infrared Thermography (IRT)	Diminishing Round Thermal Elevation on midriff skin surface
Saxena, Ng, Mathur et al. [31]	Effect of carotid artery stenosis on neck skin tissue heat transfer	With the increase in the carotid artery stenosis, a quantitative change, the presence of a colder region called 'cold feature', in external neck skin temperature features was reported
Ley and Kim [37]	Determination of atherosclerotic plaque temperature in large arteries	As blood velocity increases, the convective cooling effect is reduced with increasing the size of flow circulation over plaque/lumen surface.

The outcomes of this study will significantly improve the reliability of IRT as a clinical diagnostic tool to detect AAA. Based on Planck's radiation law, infrared temperature measurement of subject is captured using a non-contact infrared thermography sensor [30]. Utilising IRT, the temperature differences on the target subject from infrared radiation emission are visualised as a heatmap. The thermography of target objects in the thermal image are useful in clinical detection of various diseases such as stenosis of carotid artery [13,31–34]. To add on, another example of thermography application is complimentary diagnostic of early wound infection due to Caesarean section by identifying cold spots on abdominal thermography [35]. Consequently, the non-invasive, non-ionising, non-contact imaging approach [36] in measuring the distribution of the abdominal skin surface temperature would potentially improve the rate of early diagnosis treatment.

Firstly, an in-depth CFD rigid-wall Analysis was conducted in this study to simulate clinical environments and regular body temperatures to understand the correlation between transient CTP with AAA and midriff skin surface. To illustrate the difference, comparison of CTP of AAA and healthy abdominal aorta was presented. Next, the temperature (isotherm) contour of midriff skin surface was examined and correlated with the CTP. Additionally, isotropic AAA was simulated in this FSI Analysis due to anisotropic simulation limitations. As such, these facilitated the comparison of CTP of AAA and temperature contour of midriff skin surface from CFD rigid-wall and FSI Analysis.

Table 1 lists all literature that were relevant to the objectives of this study. Existing literature did not study the bioheat transfer effect of AAA onto the midriff skin surface using FSI Analysis. In

Section 4, the findings from this study would be compared with existing literature as research on bioheat transfer of artery and CTP are still in infancy stage.

2. Methodology

To draw comparison between CFD rigid-wall and FSI Analysis, identical simulation setups were set for both analyses. The methodology for CFD rigid-wall Analysis was not detailed in this study as it was covered in previous study [14]. Nevertheless, it is similar to the methodology of CFD solver in FSI Analysis detailed in Section 2 with the exception of dynamic mesh setting.

2.1. Model setup

The synthesis of this study was done according to the CFD solver's numerical simulation setup, boundary conditions, physical and thermal properties detailed in Ng and Pang [14] to ensure the validity of numerical simulation setup. For consistency and reliability of the results, identical setups including but not limited to pressure based and transient solver, *k-ω* Shear Stress Transport (SST) model, Semi-Implicit Method for Pressure Equations (SIMPLE) scheme, Green-Gauss Cell based spatial discretization, Second Order Upwind scheme on pressure and energy equations and residuals criteria of 1E-06 and 1E-04 (for continuity equation only) were applied at CFD solver respectively. In short, the setups were tightly controlled such that all numerical simulation setup, solution algorithm, boundary conditions and models used were identical. To validate the replication of setup, the deviations of maximum, minimum and average static temperatures of abdomen midriff skin surface with the results from Ng and Pang [14] study were ensured to be below deviation rule of thumb which stands at 0.5%.

In FSI Analysis, the intraabdominal pressure exerted forces to the solid interface boundary such as AAA wall, resulting in a deformation of structure. Consequently, displacement was resulted on the fluid domain (blood). On the other hand, hemodynamic forces from the transient and pulsatile blood flow were exerting on the solid domain (AAA wall). The two-way feedback of structural deformation of solid domain onto fluid domain and hemodynamic forces of transient pulsatile fluid domain onto solid domain were modelled as two-way FSI on commercial simulation management software, ANSYS Workbench (Version 2021 R1) on a 48-cores Intel® Xeon® Platinum 8358 @ 3.60 GHz workstation.

Before importing the geometry to both ANSYS Transient Structural (FEA solver) and Fluent (CFD solver), an artificial thickness was added to the patient-specific's AAA model generated by Ng and Pang [14]. Next, the geometry mesh was generated at respective solvers. AAA and abdominal tissue mesh was generated at both FEA and CFD solvers. However, blood mesh was generated in CFD solver only. Individual solver's setup was established in accordance with the boundary conditions (discussed in Section 2.5) and respective physical and thermal properties (discussed in Section 2.6). Following which, the System Coupling component in ANSYS Workbench coupled the FEA and CFD solvers. A total time step of 4.5 s (5 cardiac cycles) was setup for the two-way data transfers between the AAA wall interfaces. To begin, the mesh displacement due to intrabdominal pressure was computed from FEA solver and transferred to CFD solver. CFD solver would then update the volume mesh dynamically in the deforming regions subjected to motion defined at boundaries based on the deformation data received from FEA solver (discussed in Section 2.7). Subsequently, the force generated from the transient blood flow was transferred to FEA solver. The coupling iteration would move on to the next time step if either the Root Mean Square (RMS) values converged or when a maximum of 20 system coupling iterations were achieved. The coupling system would terminate

when all time steps were completed. Figure 1 depicts the two-way FSI Analysis workflow. The governing equations used in the FSI Analysis were solved via the Finite Volume Method (FVM) with ANSYS Transient Structural and Fluent (Version 2021 R1).

2.1.1. Governing equations

Despite the added complications of pulsatile flow and Newtonian blood, the governing equations in this FSI Analysis are fundamentally governed by incompressible continuity and Navier-Stokes momentum equation for Fluid Domain (Eqs (1) and (2)) and momentum conservation equations for Solid Domain (Eq (3)).

Apart from utilising Navier-Stokes equations, Pennes' bioheat transfer equations (Section 2.2) and regression equation for h_c (Section 2.3) were used in this study.

2.1.1.1. Fluid domain

Arbitrary-Lagrangian Eulerian (ALE) method is commonly used in the FSI Analysis. As such, the incompressible continuity and Navier-Stokes momentum equations in ALE form are expressed as:

$$\nabla \times u = 0 \tag{1}$$

$$\rho_f \left(\frac{\partial u}{\partial t} + \left((u - u_g) \cdot \nabla \right) u \right) = -\nabla p + \mu \nabla^2 u \tag{2}$$

where, ρ_f is fluid density, p is pressure, u is fluid velocity vector and u_g is moving coordinate velocity.

The relative velocity of the fluid with respect to the moving coordinate velocity in Navier-Stokes equation (Eq (2)) was used to account for movement of the mesh [38].

2.1.1.2. Solid domain

In FSI Analysis, the AAA and abdominal tissue were simplified and modelled as non-linear, hyperelastic and isotropic material which they were assumed to experience large displacements. The momentum conservation equation expressed in Lagrangian coordinate system (Eq (3)) is commonly used to pick up the displacement of AAA and abdominal tissue resulted from the hemodynamic forces of blood flow.

$$\nabla \cdot \tau_s + f_s^B = \rho_s \ddot{d}_s \tag{3}$$

where, τ_s is solid stress tensor, f_s^B is body force per unit volume, ρ_s is density of AAA wall and abdominal tissue and $\ddot{d}_s$ is local acceleration.
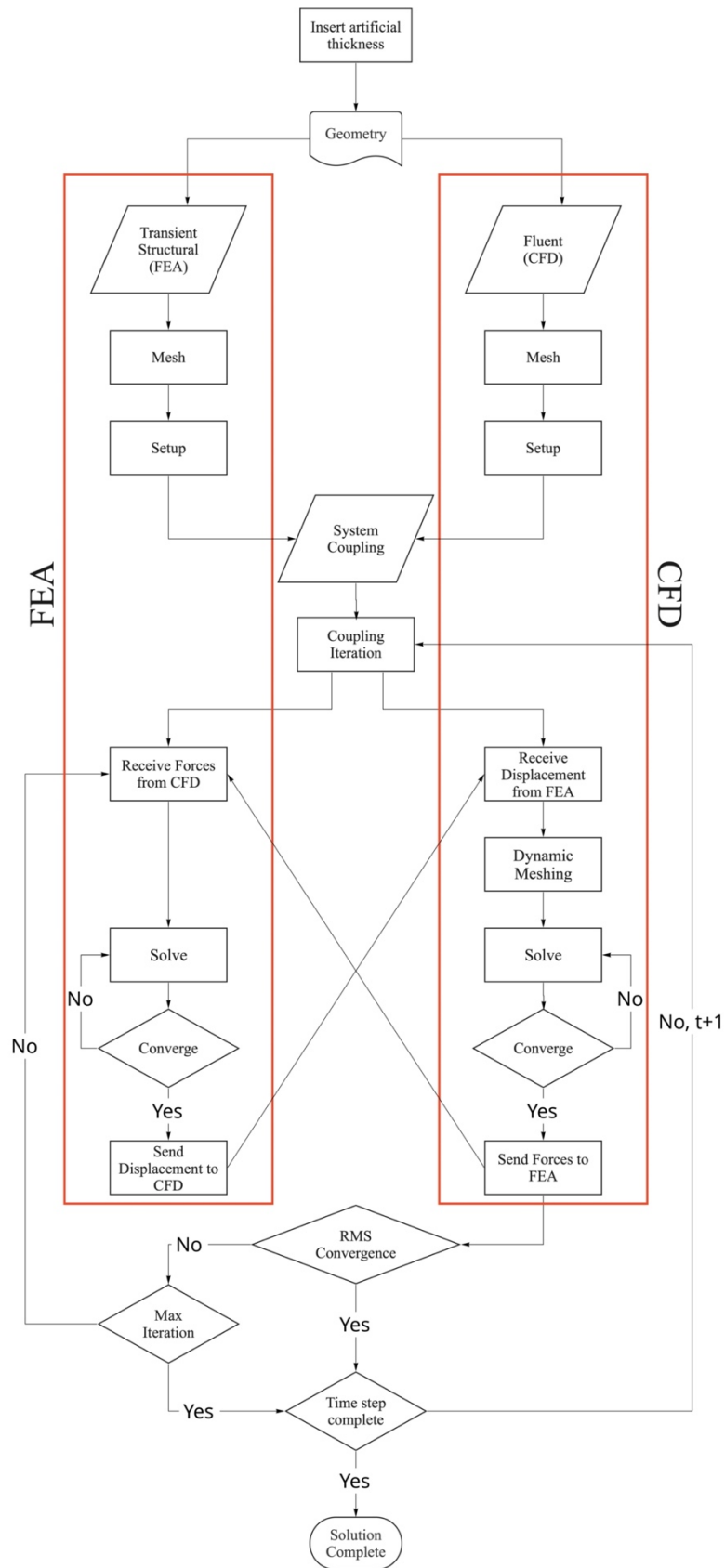
Figure 1. Coupled two-way FSI solution procedure.

2.2. Pennes' Bioheat Transfer equation

Pennes' Bioheat Transfer equation (Eq (4)) was scripted as User Defined Function (UDF) to account for the complex heat transfer process in abdominal tissue which include blood perfusion and metabolic heat generation effect. The UDF can be found in Appendix (a). Furthermore, the value for respective parameter in Eq (4) can be found in Table 4.

$$\rho_t C_{pt} \frac{\partial T}{\partial t} = k_t \left(\frac{\partial^2 T}{\partial x^2} + \frac{\partial^2 T}{\partial y^2} + \frac{\partial^2 T}{\partial z^2} \right) + \rho_t c_{pt} h_t V_t (T_{in} - T) + Q_m \tag{4}$$

2.3. Convection heat transfer

Convection heat transfer is defined as heat transfer between abdomen surface (solid) and freestream fluid (air). Most empirical average h_c which fail to consider the effect of non-convective heat transfer areas by each posture fall at 4.5 W/m²K [39]. However, it is important to realise that the deviation of overall h_c of entire body is dependent on the body posture (i.e., standing, sitting, supine etc.) [39]. For instance, the mean ratio of the convective heat transfer area to the total body surface area (mean effective thermal convection area factor) of right-abdomen and left-abdomen at supine position were 0.086 and 0.062 respectively [40]. Therefore, Kurazumi, Tsuchikawa, Ishii et al. [41] formulated a regression equation which is a function of the difference between the average surface integral mean skin temperature, $T_{s,m}$, corrected using convective heat transfer area and the local surrounding air temperature, T_a. In other words, to simulate the standard clinical diagnostic procedure, h_c, will be computed based on supine position on floor using Eq (5) in this study.

$$h_c = 0.881 \times \Delta T^{0.368} \, [W/(m^2 K)] \tag{5}$$

where $\Delta T \, [K] = T_{s,m} - T_a$.

2.4. Mesh setup

In FSI Analysis, two independent meshes were generated at FEA and CFD solvers. The two meshes were mapped for data exchanges automatically during the initialisation at ANSYS System Coupling. The high-quality mapping between the source and target meshes on coupling interface guaranteed a higher quality of data transfers. At FEA mesh, total of 119,458 tetrahedral elements were generated using combination of patch conforming algorithm, inflation at abdomen and face meshing at AAA outer and inner wall surfaces. Notably, the mesh was generated using non-linear mechanical physics for the non-linear hyperelastic property of abdominal tissue and AAA. The CFD mesh consisted of total 671,787 tetrahedral elements. Apart from inflation and face mesh on blood, both CFD and FEA utilised identical mesh techniques on the AAA and abdominal tissue, to study the thermal response of AAA and abdomen.

The interface which subjected to the motion of the dynamic zone was defined in both FEA and CFD solvers. The interface of AAA wall that in contact with the blood flow was specified as Fluid Solid Interface at FEA solver and System Coupling at CFD solver's Dynamic Mesh Zones setting respectively. This interface would exchange data (i.e., forces and displacement) at System Coupling. Other than that, stationary boundary condition was applied at Dynamic Mesh Zones setting for interfaces such as AAA inlet and outlet surface, blood inlet, abdominal top, bottom and back surfaces. Notably, these interfaces were based on assumption that there would be no deformation.

2.5. Boundary conditions

The boundary conditions at CFD solver were controlled to be identical as Ng and Pang [14] study. For instance, the transient pulsatile blood flow velocity at the aorta inlets was simulated using velocity data taken from the work by Ouriel, Green, Donayre et al. [42]. The UDF for pulsatile velocity blood flow can be found in Appendix (b). The initial inflow blood temperature was set at 310.15 K. On the other hand, the initial inflow blood pressure was set at 0 Pa gauge pressure (Figure 2 shows the inflow blood pressure in FSI Analysis). Similarly, the outlet of aorta was set as 0 Pa gauge pressure [31]. The blood flow on aorta wall was non-slip [14,43,44]. To add on, the back, top and bottom surfaces were set to be at an adiabatic boundary condition.

Contrastingly, to study transient thermal pulse wave of AAA and midriff skin surface at clinical environment, patient with regular body temperature patient (37 °C) at supine position on floor of clinical temperature (20.85 °C) was simulated. The corresponding h_c which stood as 2.4524 W/m²K was computed using Eq (5) and tabulated in Table 2. Notably, the body core temperature was assumed to be same as the average surface integral mean midriff skin surface temperature, $T_{s,m}$ in this study. On top of that, to provide a more quality comparison, AAA and abdominal tissue was subjected to the intraabdominal pressure of 239.98 Pa (1.8 mmHg) resulted from surrounding perivascular tissues at the supine position was set to simulate the pressure acting towards the abdomen skin surfaces internally and aorta wall externally [45]. Additionally, fix support was applied on both ends of AAA and top, bottom and back surfaces of abdomen, because their movements were restricted by connecting aorta, shoulders and contact surface at supine position respectively [29,46].
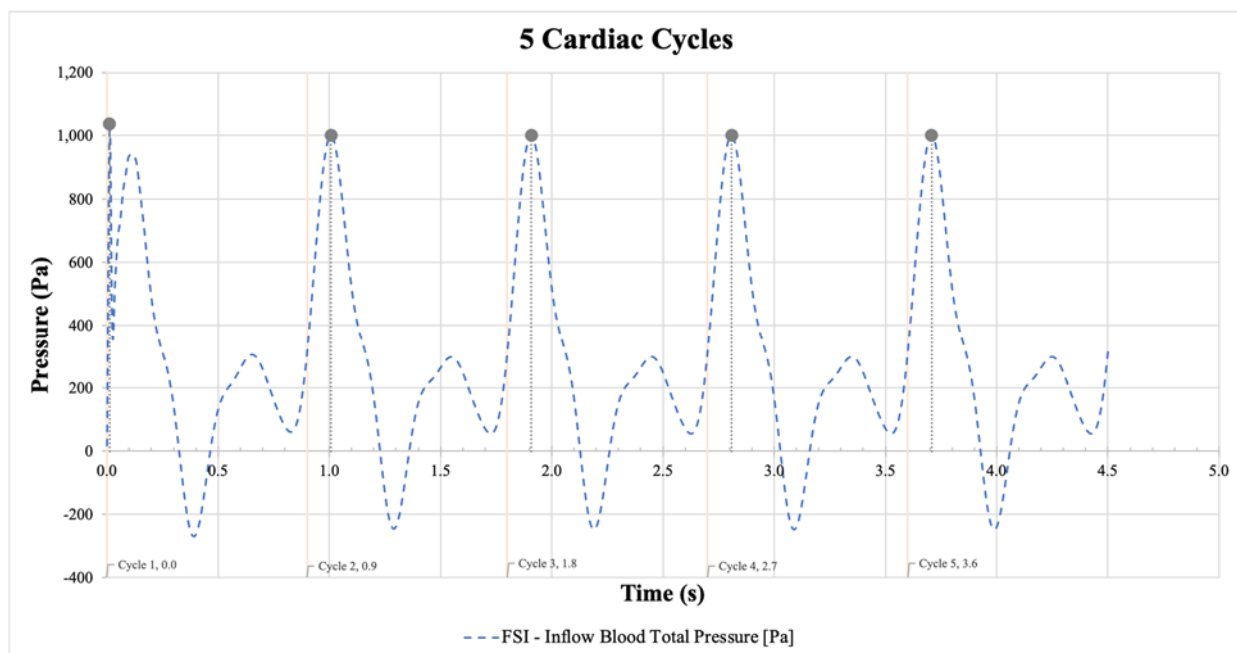

Figure 2. Pulsatile pressure waveform of 5 cardiac Cycles reproduced from [42] for FSI Analysis. The inlet peak systolic flow occurs at t = 0.012, 1.008, 1.908, 2.808 and 3.708 s for respective cycles.

Table 2. Boundary conditions of body temperature, local surrounding air temperature and respective convective heat transfer calculated using Eq (5). Assumptions made: Uniform initial temperature profile on the entire abdomen and aorta model.

Regular Body Temperature (37°C) Patient at Clinical Environment Temperature (20.85 °C)	
$T_{s,m}$, Average Surface Integral Mean Skin Temperature [K]	310.15 (37 °C)
T_a, Local Surrounding Air Temperature [K]	294.00 (20.85 °C)
h_c, Convective Heat Transfer Coefficient (Eq (5)) [W/m^{2}K] [41]	2.4524

2.5.1.   Transient velocity

The aorta inlet's pulsatile blood flow modelled by Ouriel, Green, Donayre et al. [42] was used to simulate the five cardiac cycles in both CFD rigid-wall and FSI Analysis. The first three cycles were simulated to illustrate the solutions were affected by the initial conditions as suggested by Di Martino, Guadagni, Fumero et al. [47], while the Fourth and Fifth Cardiac Cycles were used to analyse in conjunction with thermal response of models. The Pulse Cycle Independence study was discussed in Section 3.3. Next, referring to Figure 3, with the introduction of artificial thickness of 0.0015 m to AAA model and hence narrower flow path in FSI Analysis, the inlet velocity is 0.521% higher than CFD rigid-wall Analysis. In addition, five points of interest were chosen to identify the relationship between cardiac cycle and the changes in blood hemodynamic. Namely, the five points were early systole (A), peak systole (B), end systole (C), peak diastole (D) and end diastole (E). They were events that resulted in a thermal response of aorta wall and midriff skin surface. The time stamps of these five points at each cycle were plotted and tabulated in Figure 3 and Table 3.
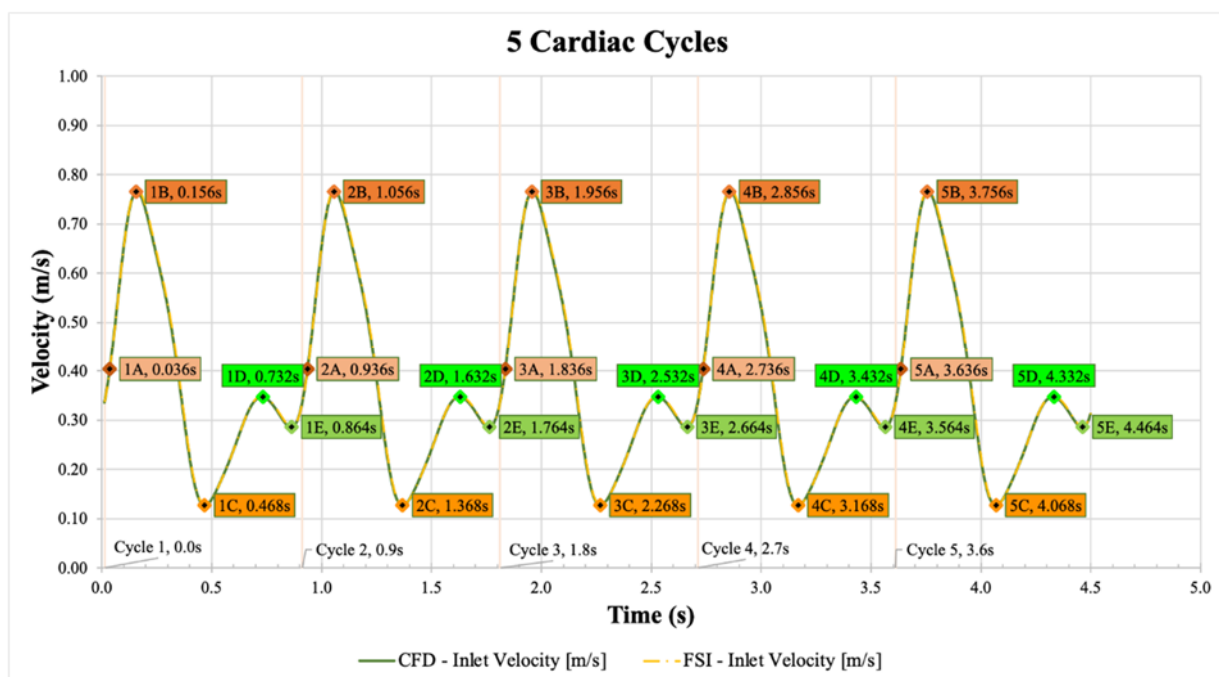

Figure 3. Pulsatile velocity waveform of 5 Cardiac Cycles reproduced from [42] for the CFD rigid-wall and FSI Analysis. There were 5 points of interest at each cycle where each point will result in changes in blood hemodynamic. They were labelled as A–E and the digit represent the cycle.

Table 3. Summary of time stamps of early systole (A), peak systole (B), end systole (C), peak diastole (D) and end diastole (E) in five cardiac cycles. To be used in conjunction with Figure 3. The digit '#' represents the cycle number.

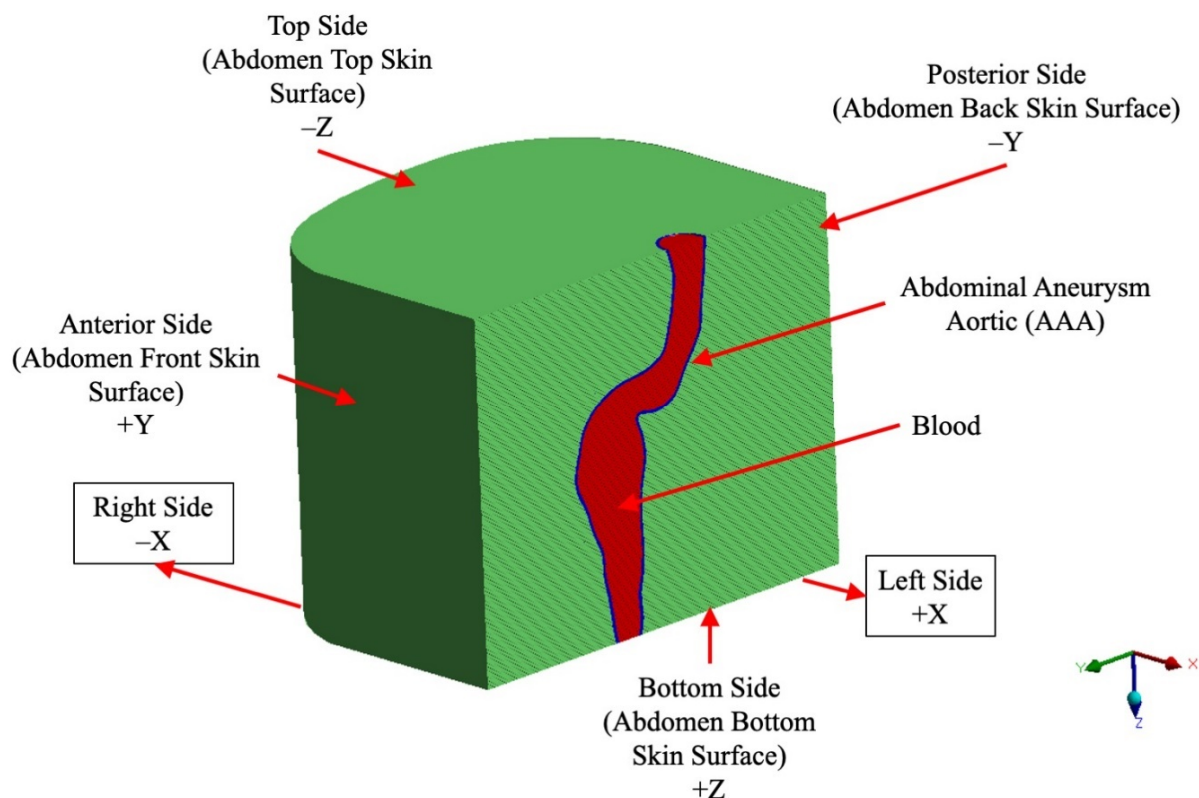| Cycle #	Start [s]	End [s]	Early Systole [s] - #A	Peak Systole [s] - #B	End Systole [s] - #C	Peak Diastole [s] - #D	End Diastole [s] - #E
Cycle 1	0.0	0.9	0.036	0.156	0.468	0.732	0.864
Cycle 2	0.9	1.8	0.936	1.056	1.368	1.632	1.764
Cycle 3	1.8	2.7	1.836	1.956	2.268	2.532	2.664
Cycle 4	2.7	3.6	2.736	2.856	3.168	3.432	3.564
Cycle 5	3.6	4.5	3.636	3.756	4.068	4.332	4.464

2.6. Physical and thermal properties

Figure 4. FSI Analysis—Model schematic (sectional view at mid-plane of abdominal tissue). Abdominal tissue (in green), AAA (in blue) and blood (in red).

The CFD rigid-wall and FSI Analysis presented herein was modelled using the similar physical properties of blood and abdominal tissues from Ng and Pang [14] unless stated otherwise.

Figure 4 illustrates the isometric sectional view of model schematic in FSI Analysis. Importantly, contrary to the rigid body assumptions in CFD rigid-wall Analysis, the AAA wall with artificial thickness (Figure 4 – in blue) and abdominal tissue (Figure 4 – in green) were flexible bodies in FSI

Analysis. Hence, they were modelled as non-linear, isotropic, hyperelastic materials using two parameters Mooney-Rivlin model [29,48]. The Strain Energy Function (SEF) is given in the model by:

$$\Psi_{iso} = C_1(I_1 - 3) + C_2(I_2 - 3) + \frac{1}{d}(J - 1)^2 \tag{6}$$

$$d = (1 - 2v)/(C_1 + C_2) \tag{7}$$

where, Ψ_{iso} is Strain Energy Density [J/m^3], C_1 & C_2 is Mooney-Rivlin Constant 1 and 2 respectively [Pa], J is volume ratio (deformed volume over the undeformed volume), I_1, I_2 are first and second invariant of the Cauchy-Green Deformation Tensor, d is material incompressibility parameter [Pa^{-1}] and v is Poisson Ratio.

Note: The constants C_1 and C_2 are denoted by C_{10} and C_{01} respectively in ANSYS Engineering Data [49].

2.6.1. Blood

For blood (Figure 4 – in red), similar blood properties were used in CFD rigid-wall and FSI Analysis. It has specific heat capacity, thermal conductivity, density and dynamic viscosity of 3650 J/(kgK), 0.51 W/(mK), 1060 kg/m^3 and 0.0035 Pa·s [34,50] respectively. Also, the blood was assumed to be laminar flow, homogenous, incompressible and Newtonian due to the large artery diameter [43,51,52].

2.6.2. Abdominal Aortic Aneurysm (AAA) model

Figure 5 represents the identical patient-specific AAA model used in CFD rigid-wall Analysis. Similar to Ng and Pang [14] assumption, the AAA at CFD rigid-wall Analysis was assumed to be a thin wall with zero thickness and rigid body property. Hence, the AAA material properties outlined in Table 4 was not applicable in CFD rigid-wall Analysis.

However, in FSI Analysis, where the AAA wall was modelled to be flexible and deformable, a constant artificial thickness of 0.0015 m [23,43,53,54] was created using SolidWorks while maintaining the outer diameter of original AAA inlet (see Figure 4 – in blue). The AAA wall's density was set to be 1120 kg/m^3 [55]. The presence of intraluminal thrombus (ILT) was ignored to simplify the analysis. In particular, due to the limited literature on thermal properties of AAA wall, the specific heat capacity and thermal conductivity of AAA wall were assumed to be same as the arterial wall [16,18] which stands at 3490 J/(KgK) [56,57] and 0.476 W/(mK) [57]. As such, the aorta wall was simulated to be incompressible, isotropic, hyperelastic and with a Poisson Ratio of 0.45 [16,23,47,58]. The material parameters for Mooney-Rivlin model were obtained from Raghavan and Vorp [29] and tabulated in Table 4.
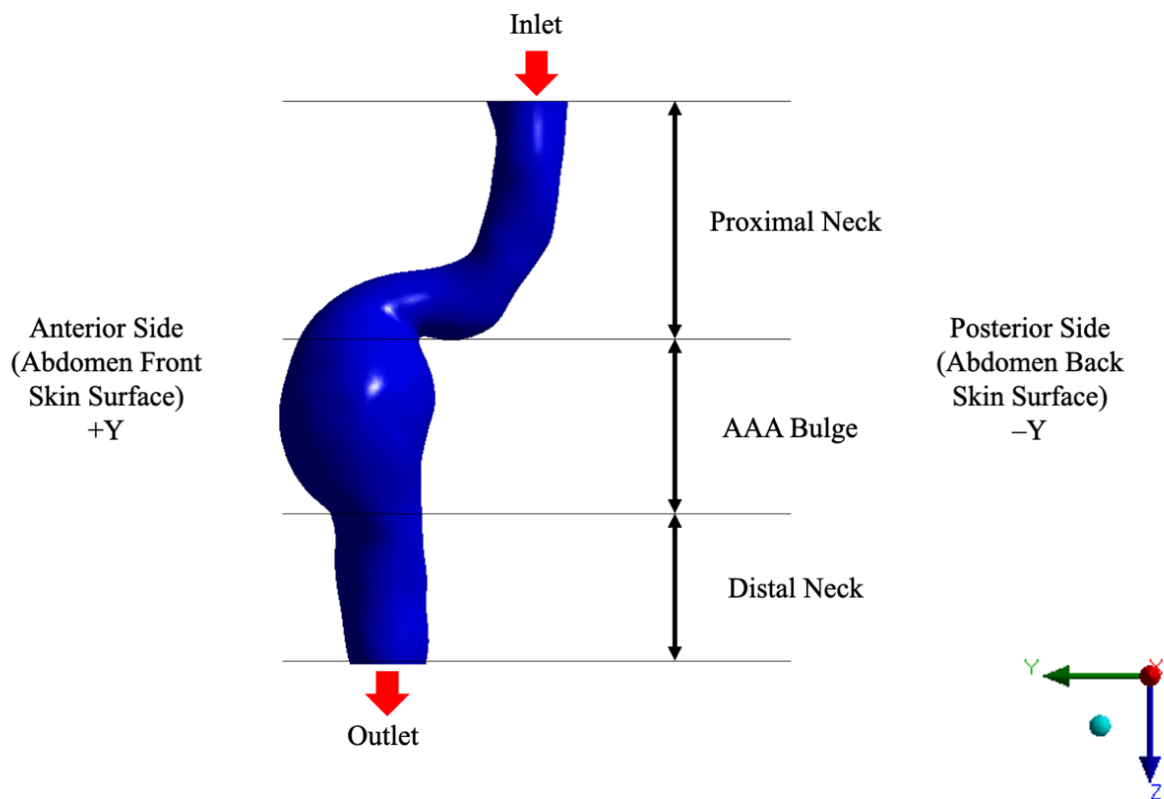
Figure 5. Patient-specific Abdominal Aortic Aneurysm (AAA) model (left side view).

2.6.3. Abdominal tissues model

In CFD rigid-wall and FSI Analysis, the specific heat capacity, thermal conductivity, density, volumetric metabolic rate, volumetric blood perfusion rate and poison ratio were 3768 J/(kgK), 0.42 W/(mK), 1085 kg/m^3, 684 W/m^3 and 0.538 /(sm^3) [59] and 0.3 [60] respectively. Similarly, the enveloping abdominal tissue around the AAA model had a volume, V_t of 0.01178 m^3.

In CFD rigid-wall Analysis, the abdominal tissue was modelled as a rigid body. However, experimental results revealed that abdominal tissue was an isotropic hyperelastic muscle [30]. The mechanical properties of abdominal tissue are complex, thereby making it challenging to conduct experiments to collect properties of abdominal tissues. On top of that, abdominal wall comprises of multiple layers of tissue with distinct properties to act as mechanical support to protect internal organs. As such, to reduce the complexity of FSI Analysis, the material parameters of Internal Oblique were used to fit the Strain Energy Function (Eq (6)) due to the inadequacy of full mechanical properties of abdominal tissue. The material parameters for the Mooney-Rivlin model were obtained from Cardoso [48] and tabulated at Table 4.

2.7. Dynamic mesh

As the AAA and abdominal tissue displace, it results in the deformation of blood flow. Thus, dynamic mesh was utilised in CFD solver to regenerate the volume mesh. Namely, the three mesh methods were spring-based smoothing, dynamic layering and local remeshing. The selection of methods was program controlled based on the remeshing requirement during coupling iterations.

Table 4. Summary of boundary conditions and physical properties of blood, AAA and abdominal tissue. Parameters introduced for FSI Analysis are labelled with a footnote "[1]" only, otherwise, the parameters are used for CFD rigid-wall and FSI Analysis.

	Blood (b)	AAA	Abdominal Tissue (t)
Boundary Conditions			
Flow Properties	Laminar, Homogenous, Incompressible and Newtonian Flow [43,51]		
Initial Inflow Temperature, T_{in} [31] [K]	310.15		
Initial Inflow & Outflow, Gauge Pressure [31] [Pa]	0		
Non-Slip [14,43]	Yes, on wall		
Heat Transfer		Coupled	Top, Bottom and Back Surfaces: Adiabatic Front Surface: Convection
Intraabdominal Pressure [45] [Pa] [1]		239.98 (1.8 mmHg)	239.98 (1.8 mmHg)
Fix Support (No Displacement) [29,46] [1]		At inlet and outlet	Top & Bottom Surfaces Back Surface
Physical Properties *(for FSI Study)*			
Density, ρ [kg/m^3]	1060	1120 [55]	1085
Mechanical Characteristics [1]		Incompressible, Isotropic, Hyperelastic [29]	Incompressible, Isotropic, Hyperelastic [48]
Thickness, t [m] [1]		0.0015 [23,43,53,54]	
Poisson Ratio, ν [1]		0.45 [23,47,58]	0.3 [60]
Volume, V [m^3] [1]		2.9099×10^{-5}	0.01178
Material Constant, C_1 [kPa] [1]		174 [29]	29.967 [48]

Continued on next page

	Blood (b)	AAA[1]	Abdominal Tissue (t)
Material Constant, C_2 [kPa] [1]		1881 [29]	12.648 [48]
Material Incompressibility Parameter, d [Pa^{-1}] [1]		4.8662×10^{-8}	9.3864×10^{-6}
Thermal Properties			
Specific Heat Capacity, c_p [J/(kgK)]	3650	3490 [56,57]	3768
Thermal Conductivity, k_t [W/(mK)]	0.51	0.476 [57]	0.42
Dynamic Viscosity, μ [Pa·s]	0.0035		
Volumetric Metabolic Rate, Q_m [W/m^3]			684
Volumetric Blood Perfusion Rate, h [1/(sm^3)]			0.538

3. Verification studies for FSI Analysis

3.1. Mesh convergence study

The CFD rigid-wall Analysis's mesh convergence study was not presented in this study because mesh sensitivity study for CFD rigid-wall Analysis was carried out exclusively by Ng and Pang [14].

The mesh sensitivity study for FSI Analysis was performed to determine the mesh setup to generate a mesh independent solution. Three mesh setups (Figure A1c)), namely: coarse, fine and finest were adopted for the mesh convergence study. The number of elements for the respective mesh setups are tabulated at Table 5. The mesh convergence study was considered acceptable as the difference in the surface area-average temperature of abdomen front surface at fifth cardiac cycle (3.6 s) from a denser mesh was less than 5% [23]. Referring to Table 5, the differences ranged from 3.2×10^{-5}% to 3.4×10^{-5}%, therefore, the solutions were considered mesh independent. In contrast with CFD rigid-wall Analysis, where coarse mesh size was chosen to save computing time, a finer mesh in FSI Analysis reduced the mesh-to-mesh interpolation between CFD and FEA solvers. Hence, the data exchange between CFD and FEA solvers converged relatively faster to provide an accurate answer. Therefore, the results generated from fine mesh in FSI Analysis were analysed and discussed in Section 4.

---

[1] Properties introduced for FSI Analysis only.

Table 5. Mesh convergence study. To be used in conjunction with Figure A1.

Mesh Size	Overall Patch Conforming Mesh (Abdomen) [m]	AAA Face Mesh [m]	Number of Elements		Computing Time [hours]	Surface Area-Average Temperature of Abdomen Front Surface at 3.6 s [K]	Difference [%]
			FEA solver	CFD solver			
Coarse	0.0300	0.0025	83,971	237,011	10.8031	310.1383	–
Fine	0.0250	0.0020	94,301	365,349	8.27806	310.1384	3.4×10^{-5}
Finest	0.0200	0.0015	119,458	671,787	10.3881	310.1385	3.2×10^{-5}

3.2. Convergence criteria

3.2.1. FEA solver

Default programme-controlled convergence criterion was set for force convergence and displacement convergence respectively. The solution computed in FEA solver converged when the force and displacement residual is lower than the convergence criterion at the end of each time step. Figures A2 and A3 demonstrated that both the parameters converged after few iterations before proceeding to next time step.

3.2.2. CFD solver

The convergence criteria at CFD solver were set to be 1E-06 for all equations, including x-, y-, z- velocity, energy, k and omega equations. In addition, the criteria of 1E-04 was set for continuity equation (Pressure based continuity equation). Each time-step was set to have a maximum 1000 iterations to provide sufficiently small linearisation error. The solver will stop iterating upon reaching these target residual convergence criteria. Figure A4 depicted the convergence of all equations at each iteration. The total iterations used for the entire analysis were estimated to be 60,000 iterations, which was below the set total iteration of 375,000 for 375 time-steps. Hence, the solution errors were minimised to an acceptable level before moving to the next time step.

3.2.3. System coupling

The accuracy of FSI Analysis was determined by the RMS convergence. The convergence of two successive iterations indicates the quality of data transfers between CFD and FEA solvers. The new coupling time step would be initiated when the RMS value of two-way data transfers fall below the default target convergence value of 0.01. The RMS change in data transfers was shown to be converged (Figure A5). The highest RMS change value was registered by Fluid: Structure to Fluent data transfer, and it fell below the acceptable target value of 0.01. Therefore, the solution converged in the two-way data transfer.

3.3. Pulse cycle independence study

We analysed the dependency of solution to boundary conditions in the first three cycles. From Figures 6 and 7, the occurrence of thermal response in term of both thermal amplitude and time stamp were inconsistent throughout the five cardiac cycles such as there was no thermal fluctuation (H1A, see Figure 6) in response to the early systole (1A) in the first cycle. On the other hand, at Figure 7,

points AA, AB and AC did not occur in a periodic manner after the occurrence at first cycle. Thus, due to the inconsistency in the thermal response, the first three cycles would not be analysed.

On the contrary, the fourth and fifth Cardiac Cycles show periodic response with constant phase shift and amplitude at each cycle, and they demonstrated steady thermal response state across all cases. It can therefore be assumed that numerical computational on geometrically similar model requires at least four continuous iterations to produce an accurate real-world representative of thermal response and damp out the initial transient result [5]. Hence, the analysis of this study will be conducted using results from fourth and fifth cardiac cycles.
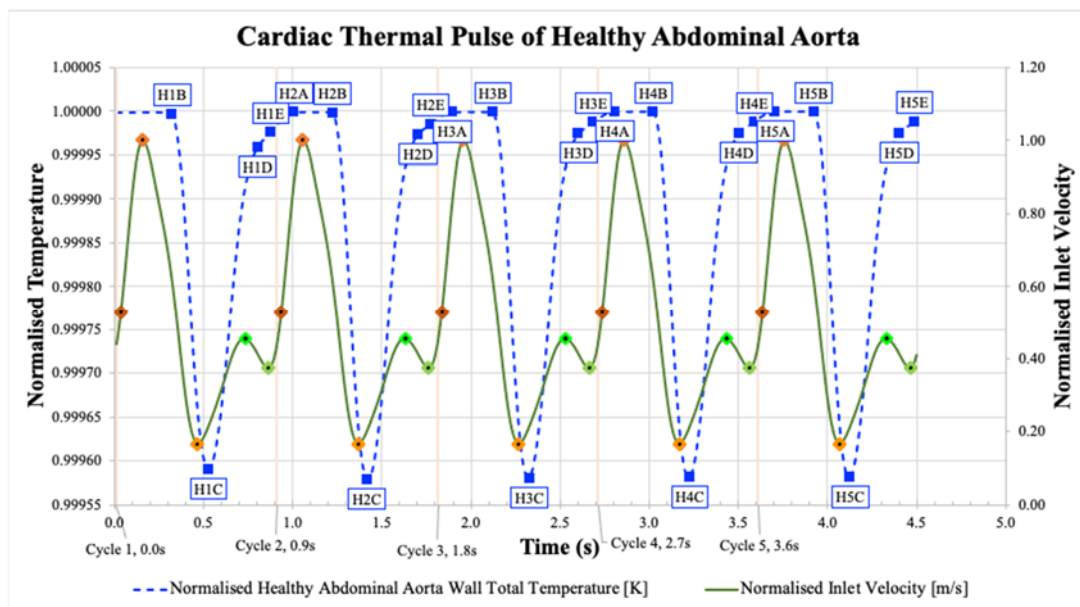
Figure 6. Five cycles CTP of healthy abdominal aorta in CFD rigid-wall Analysis. The area average total temperature at AAA wall was normalised in this plot.
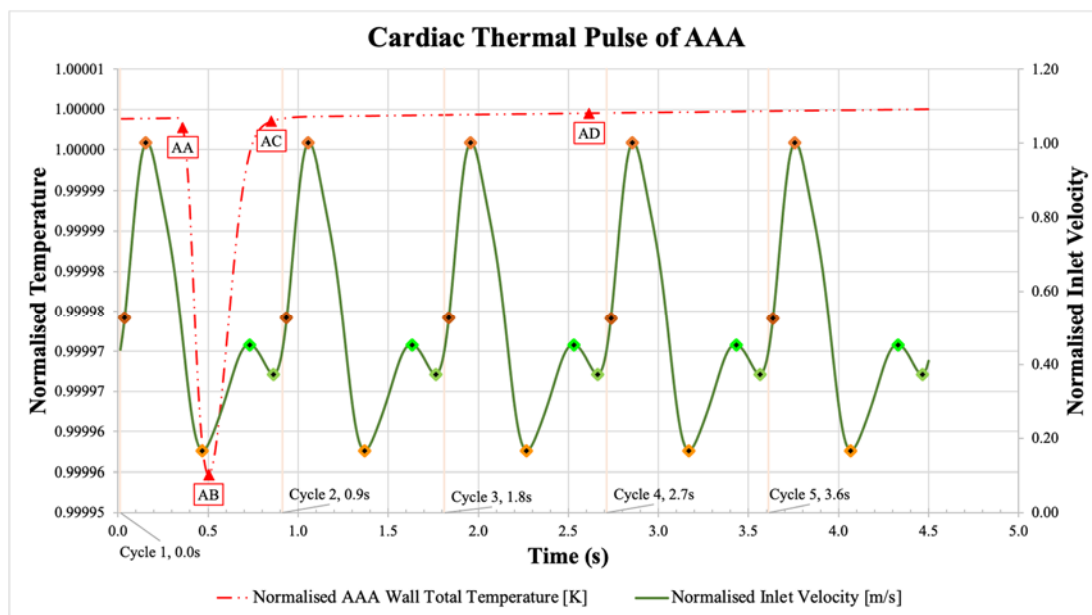
Figure 7. Five cycles CTP of AAA in CFD rigid-wall Analysis. The area average total temperature at AAA wall was normalised in this plot.

4. Results and discussion

4.1. Transient CFD rigid-wall Analysis

In this section, the results generated from CFD rigid-wall Analysis were used to study the thermal responses of AAA under the simulated boundary conditions represent in Table 2 at lower convective heat transfer coefficient, h_c.

4.1.1. Pulsatile cooling thermal profile

A pulsatile cooling thermal profile was observed at the AAA distal neck near to the left-rear outlet of aorta (Figure 5). There were two waves of cooling thermal pulse where the time occurrence did not associate with the partial CTP discussed in Section 4.1.2.2 (Table 8).

The first wave of cooling thermal pulse was stronger than the latter. The first wave of cooling thermal pulse initiated 0.264 s after peak systole (4B) (Figure 8(a)) and reach its' peak at 3.204 s (Figure 8(b)). During this wave, the AAA experienced a momentarily cooling due to the high velocity of blood flood at peak systole (4B). This wave diminished at 0.096 s before peak diastole (Figure 8(c)). The delay of thermal response to systolic phase was in part, a result of energy loss of the long-distance blood flow and the bending at the proximal neck. The overall AAA wall temperature was lower following the first wave.

The second wave was initiated at 3.348 s (Figure 8(d)), 0.012 s after the end of first wave. As the second wave's peak of cooling thermal pulse reached 0.012 s after peak diastole (4D) (Figure 8(e)), the overall local temperature of AAA wall was higher than the first wave. This can be explained in two ways: Firstly, diastolic phase did not produce significant cooling effect as compared to systolic phase; Secondly, the blood flow velocity at diastolic phase was slower than systolic phase.

In summary, the pulsatile cooling thermal profile initiated after peak systole at the left-rear outlet edge repeated in a periodic pattern over each cardiac cycle, to initiate the cooling of AAA wall. The cooling effect was more prominent at systolic phase. One of the contributing factors could be the relatively higher outlet flow velocity due to recirculation [14], which cooled the small portion of outlet distal neck. As such, the convective cooling was higher [37]. Moreover, heat transfer was observed to take place at distal neck (outlet) of AAA and it was relatively higher at the downstream of the expansion of aorta [61]. Adding on, the pulsatile cooling thermal profile was more pronounced at left-rear edge outlet since the velocity of flow was recirculated. Hence, asymmetrical pulsatile thermal cooling profile was observed due to the bending of AAA bulge.

From this analysis, it was obvious that there were thermal fluctuations, ranging to 0.0165 K, at the distal neck of aorta. The maximum thermal fluctuations measured from CTP graph of CFD rigid-wall Analysis, which reflect the area-average of AAA, stand at 1.25E-06 K. Henceforth, this is suggestive that the area average of total temperature of AAA wall does not accurately present the CTP of AAA wall.

The results from CFD rigid-wall Analysis demonstrated pulsatile cooling thermal profile at the posterior distal neck of AAA wall (near the outlet) while the cooling thermal profile was shown to be stationary from FSI Analysis's result. This is indicative that CFD rigid-wall Analysis did not exhibit the real thermal physics behaviour of AAA. The details will be discussed at Section 4.2.3.
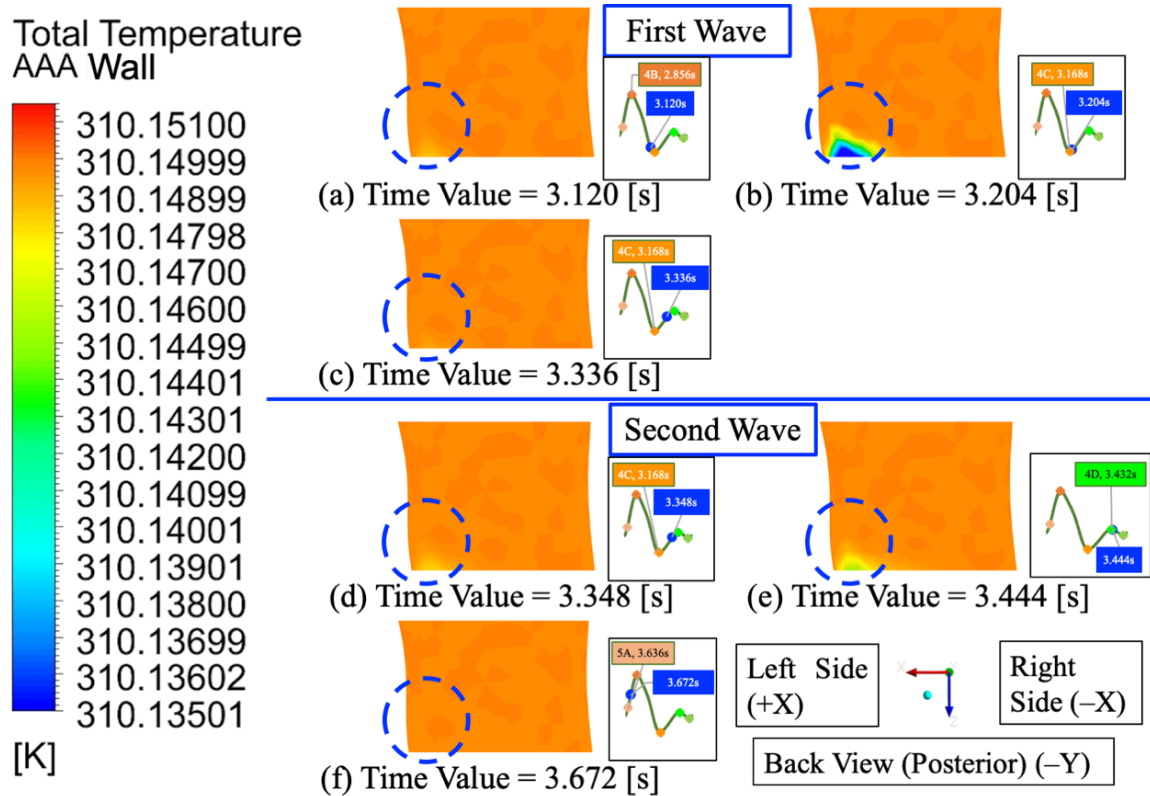
Figure 8. Back view of model to illustrate the pulsatile cooling thermal profile of posterior distal neck of AAA wall (near the outlet) of fourth cardiac cycle in CFD rigid-wall Analysis at (a) peak systole (4B) + 0.264 s (b) end systole (4C) + 0.036 s (c) end systole (4C) + 0.168 s (d) end systole (4C) + 0.18 s (e) peak diastole (4D) + 0.012 s (f) early systole (5A) + 0.036 s. Temperature contours scaled at min 310.13500 K and max 310.15185 K. To be used in conjunction with Table 3 [e.g., 0.264 s+2.856 s = 3.12 s in (a)].

4.1.2.   Cardiac thermal pulse (CTP)

CTP is defined as localised temperature fluctuations resulted from periodic physiological abdominal aortic blood flow [13]. The area-average total temperature of abdominal aorta wall and midriff skin surface were hypothesized to be cooled by the increased velocity during systolic phase as discovered by Ouriel, Green, Donayre et al. [42] and Ley and Kim [37]. The cardiac thermal response of the abdominal aorta wall was analysed and discussed in this section.

4.1.2.1.   Healthy abdominal aorta

The CTP of healthy abdominal aorta wall (Figure 9) were analysed.

In a glance, the thermal response was reacting in a pulsatile manner. Particularly, this effect was more obvious during the peak systole (4B) to peak diastole (4D) as illustrated by a sharp drop in total temperature after 0.168 s (H4B-4B) away from peak systole (4B). In addition, at 0.06 s after the end systole (4C), the temperature increased rapidly before being slowed down by peak diastole (4D) at 3.504 s in cycle 4 (Table 6).

The 5 points of interest in the cardiac cycle identified in Table 3 have different degrees of effect on the thermal fluctuations and thermal phase shift. Firstly, the thermal fluctuations were almost zero by early systole (A). Relative to this case, the highest drop of temperature was due to the peak systole

(B), and the highest spike was due to the end systole (C). The rate of increase in temperature was reduced significantly at the diastolic phase, where both peak diastole (D) and end diastole (E) reflect the same increasing rate.

As shown in Table 7, the phase shift in response to the 5 points of interest of cardiac cycle varied to a small extent. In comparison with the 0 s phase shift at 0% stenosis on neck skin surface due to peak systole (B) at neck carotid artery by Saxena, Ng, Manchanda et al. [13], the phase shift observed in this case study was relatively higher at 0.168 s. Particularly, it was also the highest phase shift in the cardiac cycle. This was partly because higher haemodynamic velocity was used in this study which resulted in higher cooling effect in the aorta wall.

In addition, the early systole (A) and peak diastole (D) resulted in similar phase shift at 0.072 s. On the other hand, at lower velocity points such as end systole (C) and end diastole (E), the phase shift was 0.06 and 0.024 s respectively (Table 7). To explain the additional delay by the effect of end systole (C), it may be contributed by higher amount of residual kinetic energy from peak systole. Also, it takes more energy to increase temperature from lower temperature. As such, the heat formation was slower.
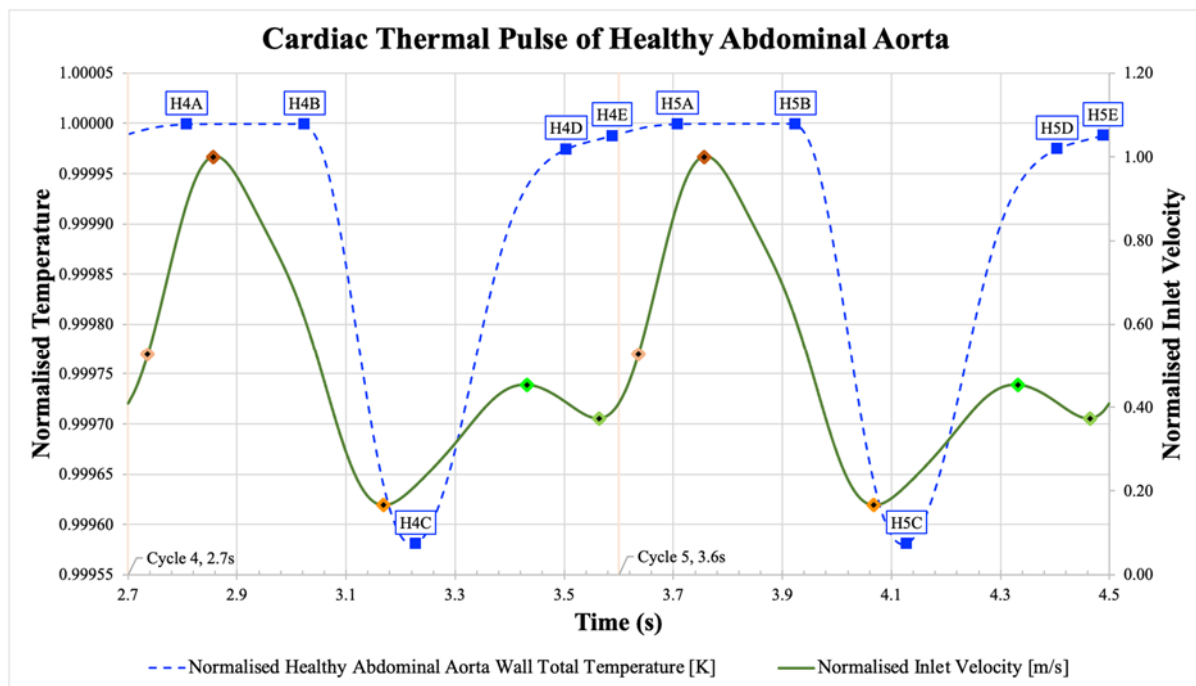

Figure 9. Fourth and fifth cardiac cycles of CTP of healthy abdominal aorta wall of CFD rigid-wall Analysis. The area-average total temperature at abdominal aorta wall was normalised in this plot. Each corresponding point associated with the five points of interest at Cardiac Cycle was labelled as H#A-E where # denotes the cycle number.

Table 6. Summary of time stamps of healthy abdominal aorta wall thermal response of CFD rigid-wall Analysis associated with early systole (A), peak systole (B), end systole (C), peak diastole (D) and end diastole (E) in fourth and fifth cardiac cycles. To be used in conjunction with Figure 9.

Cycle #	H#A [s]	H#B [s]	H#C [s]	H#D [s]	H#E [s]
Cycle 4	2.808	3.024	3.228	3.504	3.588
Cycle 5	3.708	3.924	4.128	4.404	4.488

Table 7. Phase shift between cardiac thermal response of healthy abdominal aorta wall (H#A-E) and five points of interest in Cardiac Cycle (#A-E) of CFD rigid-wall Analysis. To be used in conjunction with Figure 9.

Cycle #	H#A-#A [s]	H#B-#B [s]	H#C-#C [s]	H#D-#D [s]	H#E-#E [s]
Cycle 4	0.072	0.168	0.060	0.072	0.024
Cycle 5	0.072	0.168	0.060	0.072	0.024

4.1.2.2.   Abdominal Aortic Aneurysm (AAA)

In this section, the CTP of AAA wall (Figure 10) of CFD rigid-wall Analysis was analysed. The associated time stamps with the three points namely early systole (A), peak systole (B), end systole (C) in fourth and fifth cardiac cycles respectively were tabulated in Table 8.

In Figure 10, the thermal response demonstrated a cardiac thermal cycle in the systolic phase only. However, there was no significant impact on the temperature for the diastolic phase (4D-4E). In contrast with CTP of healthy abdominal aorta, the effect of CTP effect was less obvious in large extent especially in term of thermal amplitudes. More importantly, the effects due to diastole cycle were not visible with the presence of aneurysm. Hence, a partial CTP was observed on AAA wall in CFD rigid-wall Analysis.
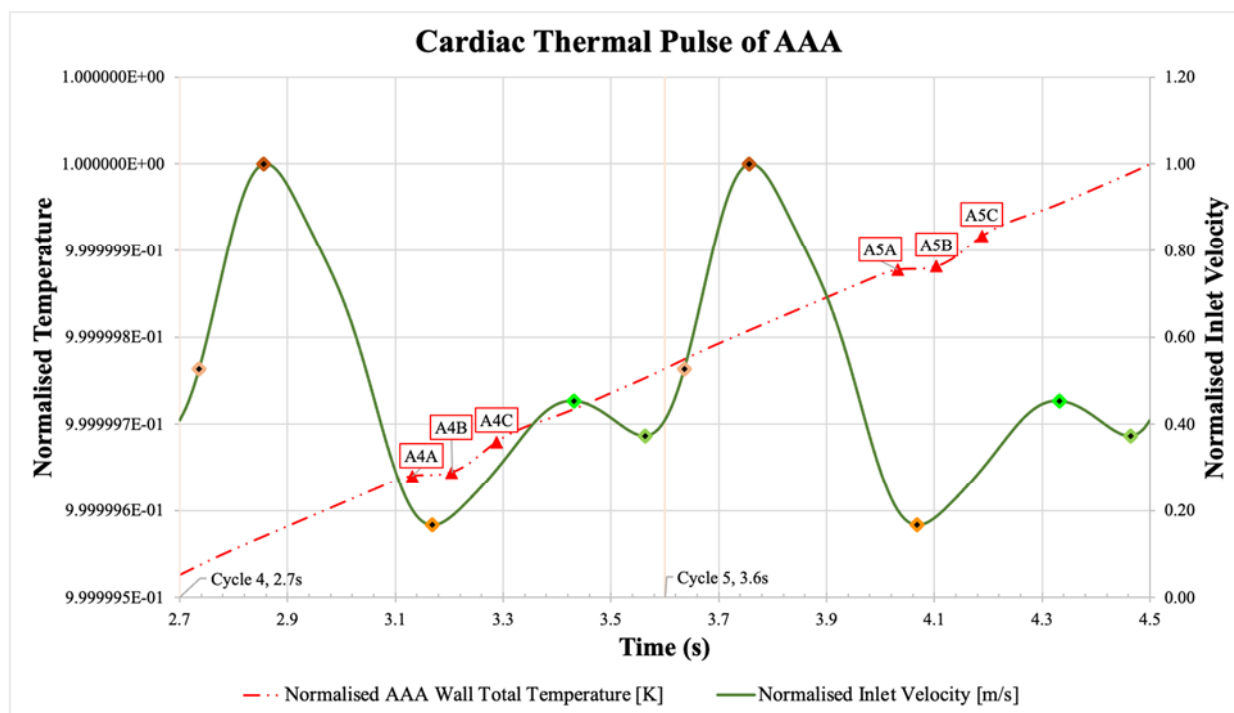

Figure 10. Fourth and fifth cardiac cycles CTP of AAA of CFD rigid-wall Analysis. The area-average total temperature at AAA wall was normalised in this plot.

Table 8. Summary of time stamps of AAA wall thermal response of CFD rigid-wall Analysis associated with early systole (A), peak systole (B), end systole (C) in fourth and fifth cardiac cycles. To be used in conjunction with Figure 10.

Cycle #	A#A [s]	A#B [s]	A#C [s]	A#D [s]	A#E [s]
Cycle 4	3.132	3.204	3.288	N.A.	N.A.
Cycle 5	4.032	4.104	4.188	N.A.	N.A.

4.2. Transient FSI Analysis

In this section, the results generated from FSI Analysis were used to compare with CFD rigid-wall Analysis to highlight the improved accuracy of thermal responses of AAA, with the implementation of more realistic boundary conditions such as the hyperelastic non-linear AAA property, constant artificial AAA wall thickness and intraabdominal pressure.

4.2.1.　Transient velocity streamlines

In this section, the transient blood velocity streamlines due to the deformed AAA wall in FSI Analysis were discussed. In addition, associated time stamps which were observed to exhibit change of average deformation trend was denoted in Figure 13.

In Figure 11, initiation of recirculation of blood flow was associated with D4B1. As the time increases, the recirculation velocity slows down due to the loss of kinetic energy. The velocity increased again at D4D (3.480 s) after the peak diastole. The velocity streamlines illustrated the deformed blood flow as a result of the deformed AAA wall during cardiac cycle. In general, recirculation was observed at the AAA bulge and it is consistent with the observations by Lin, Han, Bi et al. [17].

4.2.2.　Pulsatile structural deformation

The deformation of AAA wall due to both intraabdominal pressure and force generated from blood flow in FSI Analysis, were discussed here. Associated time stamps which were observed to exhibit change of average deformation trend was labelled in Figures 11 and 13. AAA was deformed from the original position (Figure 13 total deformation contour – shaded region) at the start of blood flow due to the intrabdominal pressure. Notably, the largest deformation occurs at the bulge area of AAA. Moreover, it was observed that the strain direction was toward the anterior side. This is consistent with the observations of Lin, Han, Bi et al. [17].

In Figure 11, the total deformation on AAA wall behaved in a pulsatile motion similar to human heart. This was partly due to the force generated from the pulsatile blood flow. In particular, the deformation at D4B1 and D4B2 were highest in the fourth cycle. This phenomenon could be caused by the initiation of blood recirculation after peak systole (4B and 5B). The higher velocity of recirculating blood flow resulted in a higher deformation at D4B2 (Figure 13c)) and D5B2. In addition, the lower deformation at D4C1 and D5C1 were associated to the low velocity of recirculating blood at the end systole (4C and 5C). D4C2 and D5C2 suggested that the deformation was further amplified by the increase of blood flow velocity, which resulted in higher force acting towards AAA wall. At the end of full cardiac cycle, the AAA wall experienced the lowest deformation at 3.624 s (D4E) due to high recirculation and low velocity at AAA bulge [62].
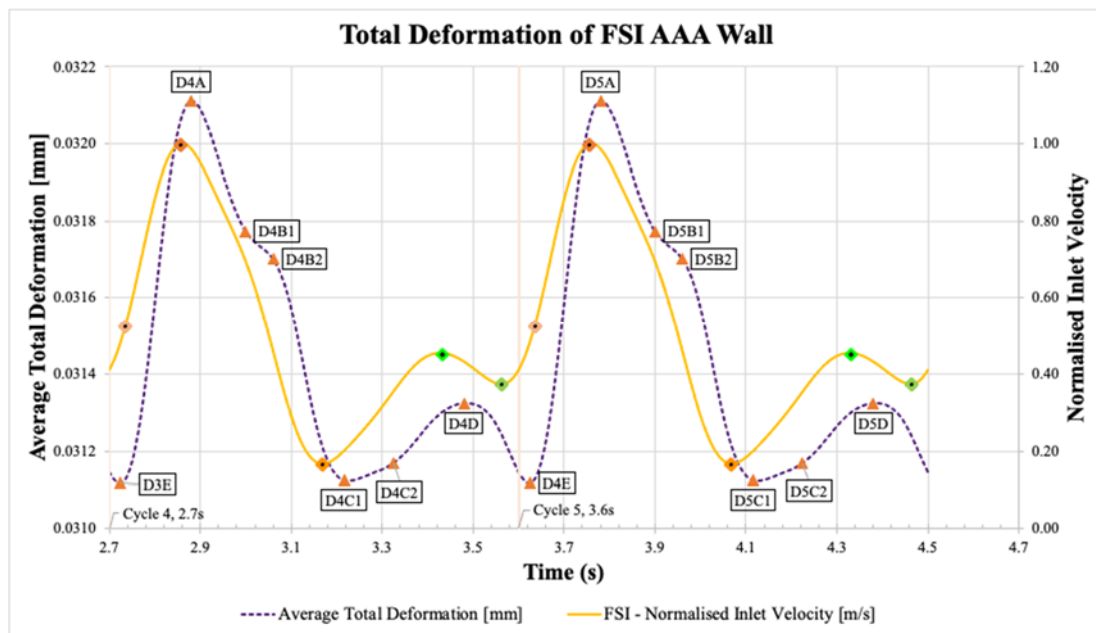
Figure 11. Average total deformation of AAA wall in FSI Analysis.

4.2.3. Thermal response of abdominal aortic aneurysm wall

In this section, the thermal response of AAA wall in FSI Analysis was analysed.

In Figure 12, the thermal response of AAA in FSI Analysis can be approximated using a 3 degrees polynomial function of $T = -2\text{E-}08\,t^3 + 2\text{E-}07\,t^2 - 8\text{E-}07\,t + 1$. In contrast to CFD rigid-wall Analysis, a CTP responded in systole phase only (Section 4.1.2.2). Thence, the thermal response reacting to the systolic phase in CFD rigid-wall Analysis was absent in FSI Analysis (Figure 12). This is justifiable as the small magnitude of temperature drop of blood ranging from $-1.25\text{E-}06$ K (A4A-A4B) to $1.09\text{E-}05$ K (A4B-A4C) diminished in the form of heat conduction in the AAA volume body. In addition, the temperature of AAA observed in the FSI Analysis (Figure 12) was marginally lower with an average difference of $-1.8641\text{E-}06$ K.

Contrary to expectations, results from FSI Analysis did not support the hypothesis of longer phase shift of AAA. Thus, phase shift of CTP at AAA would not be a good indicator to identify the degree of aneurysm. Nevertheless, this finding implies that the absence of CTP and polynomial increasing thermal response may be potential indicators to demonstrate the presence of AAA.

In the final part of the analysis on thermal response of FSI AAA, a striking observation emerged from the comparison of temperature contour of AAA illustrated in Figures 8 and 13. Comparing to earlier findings in CFD rigid-wall Analysis (Section 4.1.1), no evidence of pulsatile cooling thermal profile was detected at the posterior distal neck of AAA wall (near the outlet). The stationary cooling thermal profile was found to be at the left side of distal neck of AAA wall (near the outlet) instead. This inconsistency may be due to the consistently high velocity blood flow resulting from recirculation, indirectly generating a higher cooling effect. Moreover, an implication of the location change of cooling thermal profile may be due to the plausibility of deformed blood flow. In addition, as discussed in Section 4.1.1, the heat transfer at distal neck (outlet) of AAA was relatively higher at the downstream of the expansion of aorta [61].

Overall, these results indicated that it is possible, therefore, that CFD rigid-wall Analysis might be unsuitable to study the thermal physics of AAA due to highly deformed AAA and blood flow.
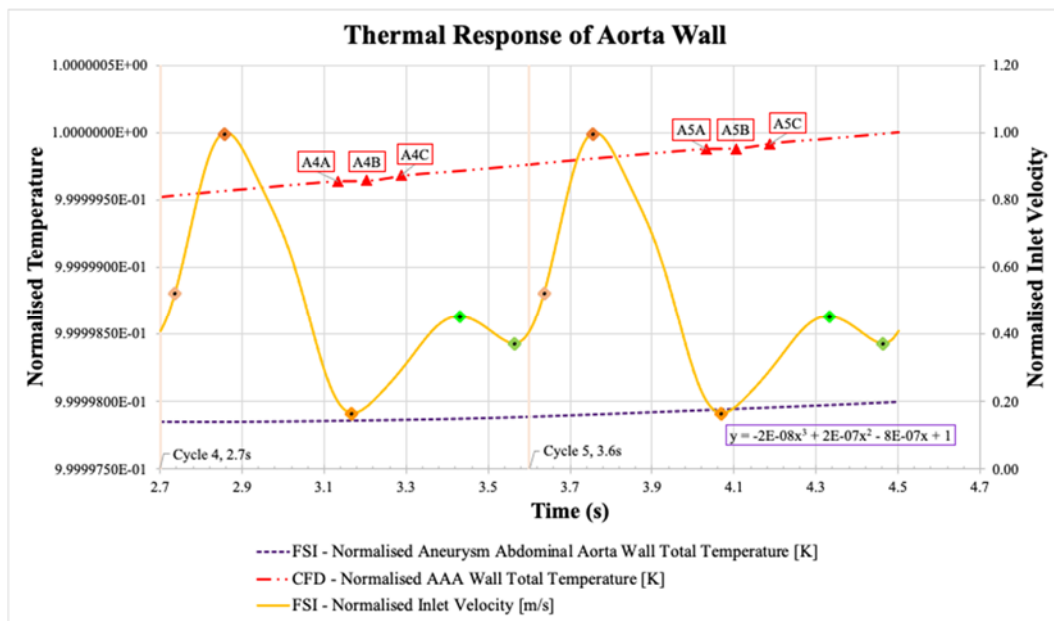
Figure 12. Comparison of AAA wall thermal response between CFD rigid-wall and FSI Analysis at Fourth and Fifth Cardiac Cycles. The area-average total temperature of AAA wall was normalised in this plot.

4.3. Thermal response on midriff skin surface of AAA

A qualitative comparison of the thermal response on midriff skin surface with Saxena, Ng, Mathur et al. [31], Ng and Pang [14] and Saxena, Ng, Manchanda et al. [13] studies was discussed in this section.
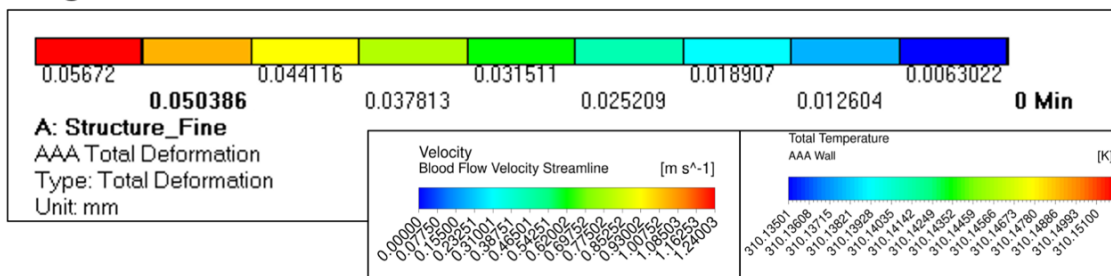
Drawing parallels with the three studies, the isotherms contour of midriff skin surface aligned with Ng and Pang [14] in two aspects. Firstly, CTP was not observed on the midriff skin surface. Secondly, a circular thermal signature was observed.

4.3.1.   Thermal gradient

Thermal gradient is the linear thermal response used to quantify the heat transfer on the midriff skin surface. The thermal gradient of each case was tabulated in Table 9 and presented in Figure 14 to illustrate the relationship between cardiac cycle and isotherms profile of midriff skin surface.

A thermal gradient was observed on midriff skin surface in all cases of this study (Figure 14). It was similar to those reported by Ng and Pang [14] despite a lower h_c of 2.4524 W/(m^{2}K) was used in this study. Notably, the thermal gradient of FSI Analysis was consistent with that of CFD rigid-wall Analysis. However, in spite of a more realistic approach used in the FSI Analysis, the thermal response on midriff skin surface differed from that of Saxena, Ng, Manchanda et al. [13], who contended that CTP was presented on the neck surface due to the carotid artery stenosis. In comparison with the properties of neck tissue and abdominal tissue such as volumetric metabolic heat generation (q_m), density (ρ_t), specific heat capacity (c_{P_t}), abdominal tissue, have relatively higher values for these tissue properties. In particular, the most prominent factor was the q_m of abdominal tissue, which was 1972% larger than the neck tissue. Therefore, the thermal gradient was largely contributed by the more dominant Pennes' bioheat transfer effect of the abdominal tissue. In this way then, CTP was not detected on the midriff skin surface where the heat transfer between AAA and abdominal tissue was insignificant. In other words, the absence of CTP on the midriff skin surface may not stem from the unrealistic boundary conditions used in CFD rigid-wall Analysis.

Legend

A: Structure_Fine
AAA Total Deformation
Type: Total Deformation
Unit: mm

Velocity
Blood Flow Velocity Streamline   [m s^-1]

Total Temperature
AAA Wall   [K]

Total Deformation [mm]   Velocity Streamline [m/s]   Total Temperature [K]
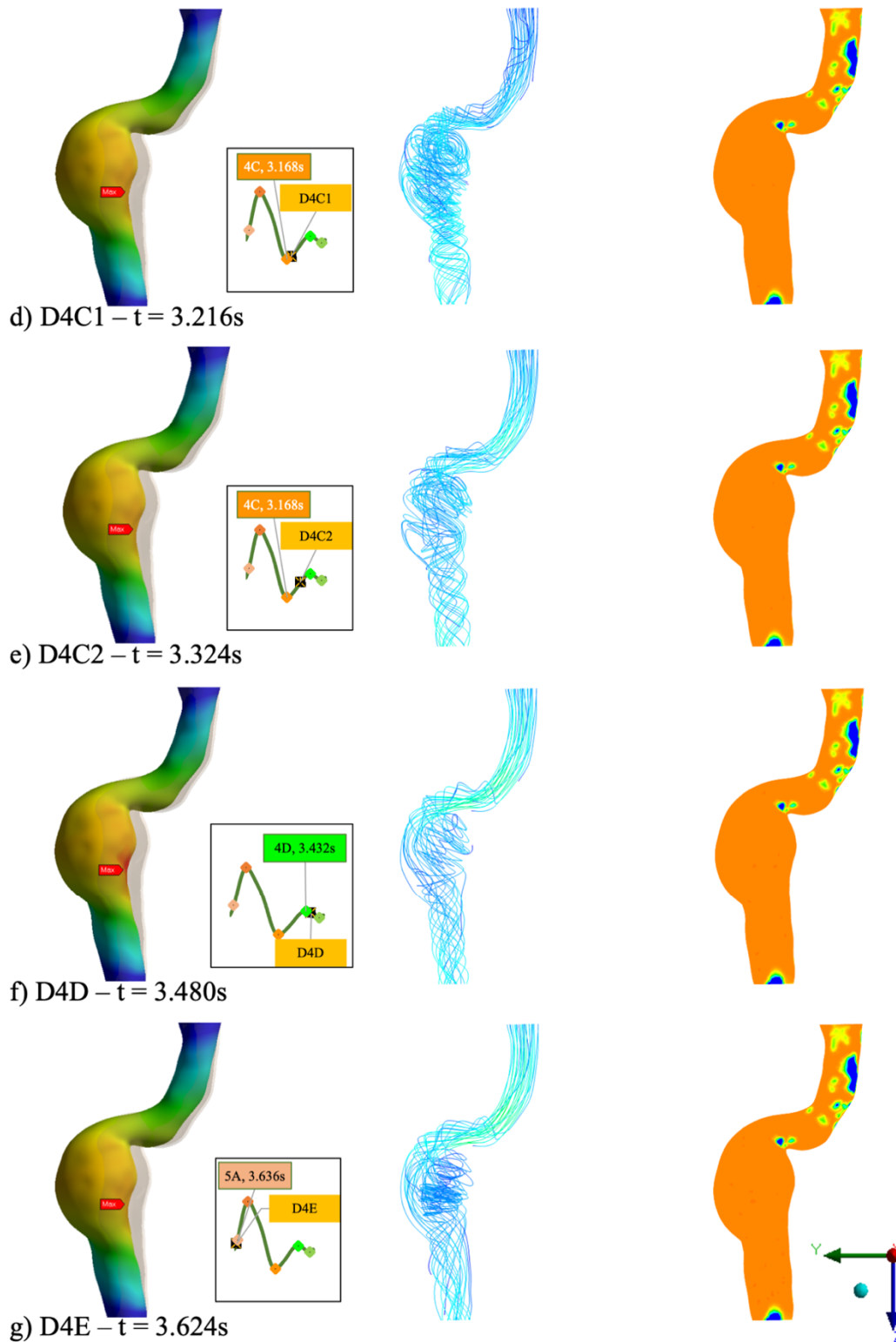
a) D4A – t = 2.880s

b) D4B1 – t = 3.000s

c) D4B2 – t = 3.060s
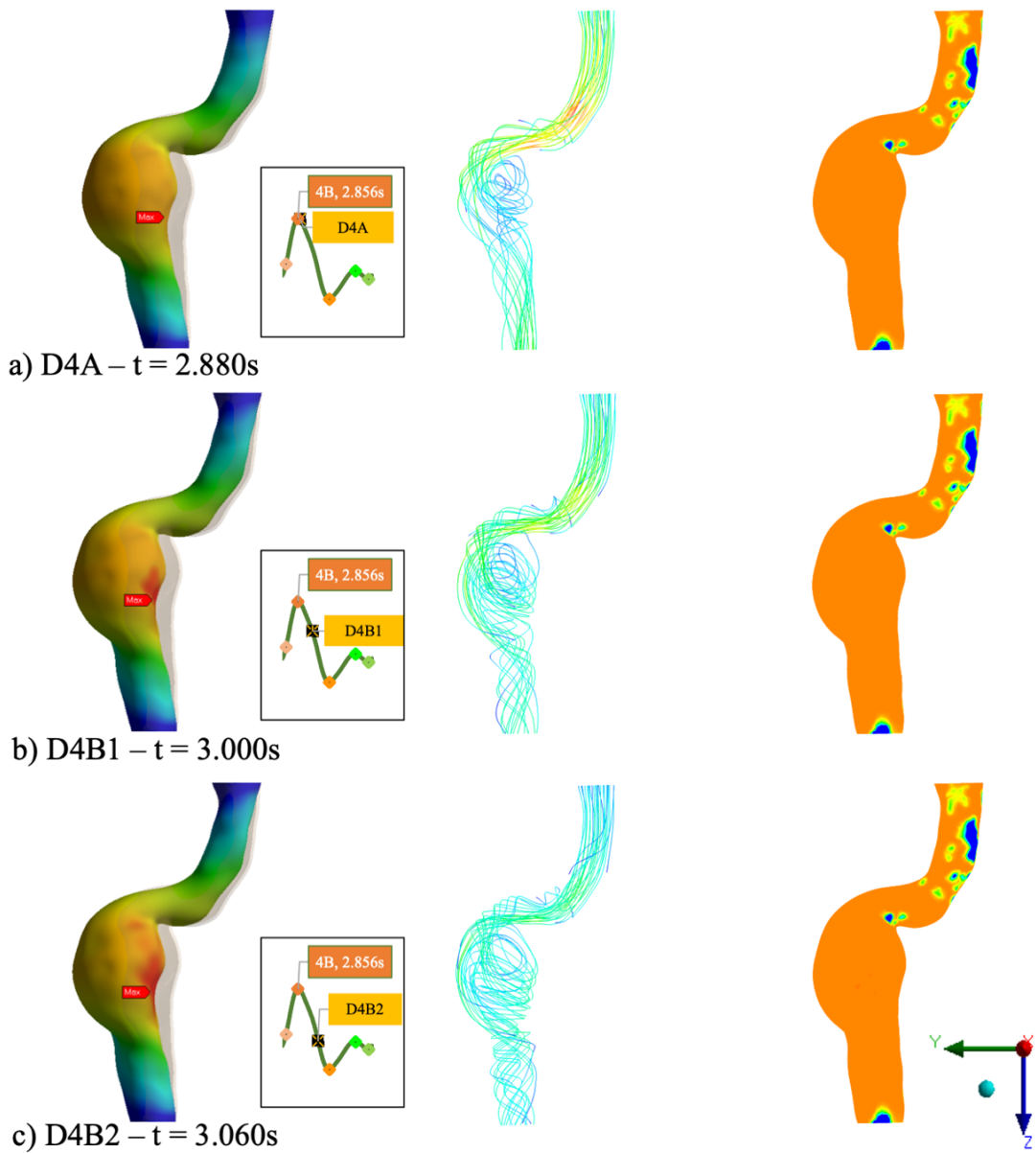
Figure 13. Total deformation (Left), Velocity streamlines (Centre) and Total temperature (Right) of left side view of AAA in FSI Analysis. Total deformation contours scaled at min 0 mm and max 0.05672 mm. Total deformation contour was plotted over the undeformed AAA (shaded). Velocity streamlines scaled at min 0 m/s and max 1.24003 m/s Temperature contours scaled at min 310.1350 K and max 310.15185 K. To be used in conjunction with Figure 11.

By comparing across thermal gradient in Table 9, the thermal effect of the healthy case was generally faster than the AAA case. To elaborate, the thermal gradient difference between AAA case and healthy case of CFD rigid-wall analysis stands at –122.22%, suggesting that AAA case was slower than healthy case. However, these results were justifiable because the cooling effect of AAA model was lower due to recirculation of flow as discussed in Section 4.1.1. In additions, by comparing across both FSI and CFD analyses, the thermal effect of AAA in FSI Analysis was observed to be faster than the CFD rigid-wall Analysis. Referring to Table 9, the difference of rate of change in total temperature of midriff skin surface for FSI Analysis was –11.11%. In comparison to healthy case, the thermal gradient stands at –50%, suggesting that FSI Analysis was slower than healthy case in CFD rigid-wall Analysis. The –11.11% thermal gradient difference between CFD and FSI analyses may imply that CFD rigid-wall Analysis is sufficient to study the thermal pattern of midriff skin surface.

Table 9. Thermal gradient [Ks^{-1}] of midriff skin surface of healthy and aneurysm patient in CFD rigid-wall and FSI Analysis. To be used in conjunction of Figure 14.

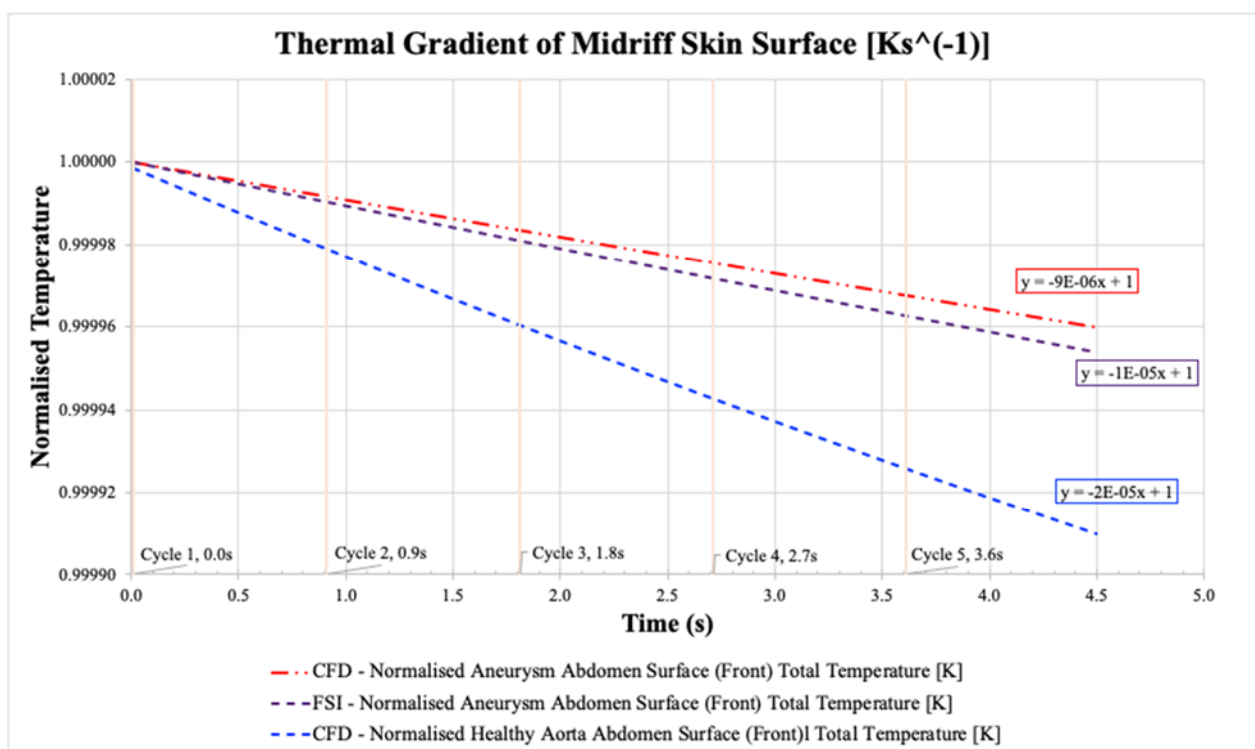|	Thermal Gradient [E-06 Ks^{-1}]	Differences [%]
Healthy (CFD rigid-wall Analysis)	–20	–
AAA (CFD rigid-wall Analysis)	–9	–122.22%
AAA (FSI Analysis)	–10	–11.11%

Figure 14. Five cycles CTP of both healthy and AAA of CFD rigid-wall and FSI Analysis. The area-average total temperature at midriff skin surface was normalised in this plot.

4.3.2. Temperature (isotherms) contour

In this section, the static temperature contour on the midriff skin surface of the AAA patient was studied to determine the effect of smaller h_c and more realistic boundary conditions in FSI Analysis.

Transient CFD rigid-wall Analysis (Section 4.3.2.1) was compared with Ng and Pang [14] to study the effect of smaller h_c while transient FSI Analysis (Section 4.3.2.2) was compared with outcomes from transient CFD rigid-wall Analysis to study the effect of more realistic boundary conditions.

4.3.2.1.   Transient CFD rigid-wall Analysis

In comparison with Ng and Pang [14] study, all boundary conditions, including initial $T_{s,m}$ and T_a were identical, with the exception that the h_c was 2.4524 W/(m^{2}K). As compared to h_c used in Ng and Pang [14] study, the h_c was 7.5476 W/(m^{2}K) smaller. As a result, the result of this study fulfils Newton's law of cooling where higher skin static temperature was recorded at lower h_c.

Further analysis showed that the temperature contour on the midriff skin surface of the AAA case reflected similar diminishing circular thermal pattern at the centre of skin surface surrounding the AAA bulge as illustrated in Figure 15. In addition, they were about the same size at the beginning of fourth cardiac cycle (systolic phase) at 2.7 s. The formation of hot-spot was partly due to the lower heat transfer between the skin surface and surrounding air. In other words, the lower h_c which result in lower heat transfer rate would be the result of higher area-average total temperature at the initial first few cycles. The lower heat transfer was proven by an estimated of 0.04 K lower minimum area-average total temperature than the case when $h_c = 10.0$ W/(m^{2}K).

Furthermore, at the end of fourth cardiac cycle (end of diastolic phase) at 3.6 s, the size of hot-spot was approximately two times smaller (Figure 15 (bottom)) due to the decrease in heat transfer from the AAA to the abdominal tissue. In short, the shrinkage in size of circular thermal elevation may be correlated to the higher cooling effect of the AAA during diastolic phase [31]. Then, as the temperature of midriff skin surface reached thermal equilibrium with the local surrounding temperature, the present of diminishing thermal elevation warrant further research.

4.3.2.2.   Transient FSI Analysis

In comparison with CFD rigid-wall Analysis, all boundary conditions, including initial $T_{s,m}$, T_a and h_c were identical, with the exception of an artificial AAA thickness of 1.5 mm and intraabdominal pressure of 239.98 Pa (1.8 mmHg) applied towards the abdominal tissue and AAA.

Further analysis showed that the temperature contour on the midriff skin surface of the AAA in FSI Analysis reflected similar circular thermal signature at the centre of skin surface surrounding the AAA bulge. In addition, the shrinkage in size of circular thermal elevation surrounding the AAA bulge was observed on the skin surface as illustrated in Figure 16. Comparing to CFD rigid-wall Analysis, the shrinkage rate of hot-spot was approximately the same. However, the temperature of hot-spot in FSI Analysis was relatively higher than CFD rigid-wall Analysis. For instance, the temperature difference at the centre of hotspot at 2.7, 3.6, 4.5 s stand at 0.0268, 0.0257 and 0.0247 K respectively. Furthermore, the hot-spot seem to be more localised in comparison with Figure 15 in CFD rigid-wall Analysis. This could be partly due to the bulge of AAA was deformed towards the midriff skin surface by intraabdominal pressure at the start of simulation. As such, this could suggest that the closer the distance of the AAA bulge to the midriff skin surface, the hot-spot would be more readily detected.
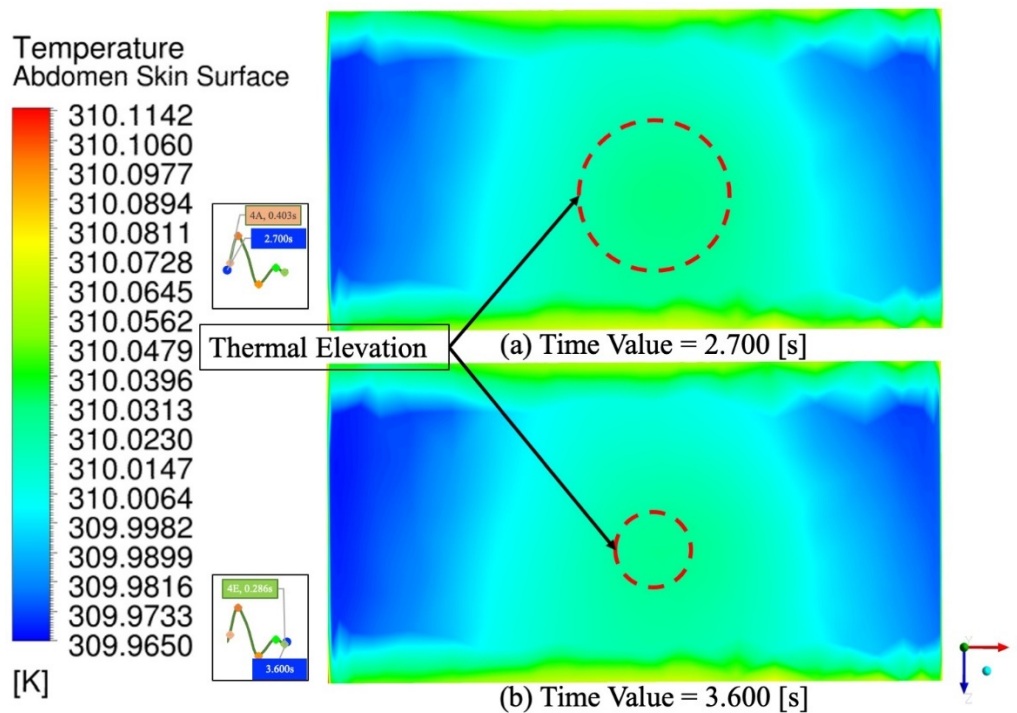
Figure 15. Temperature contours (scaled at min 309.965 K and max 310.115 K) on the midriff skin surface of the AAA midriff skin surface at the (a) start (time stamp = 2.7 s) (b) end (time stamp = 3.6 s) of fourth cardiac cycle of CFD rigid-wall Analysis. A circular thermal elevation over the bulge was observed at the centre of midriff skin surface.
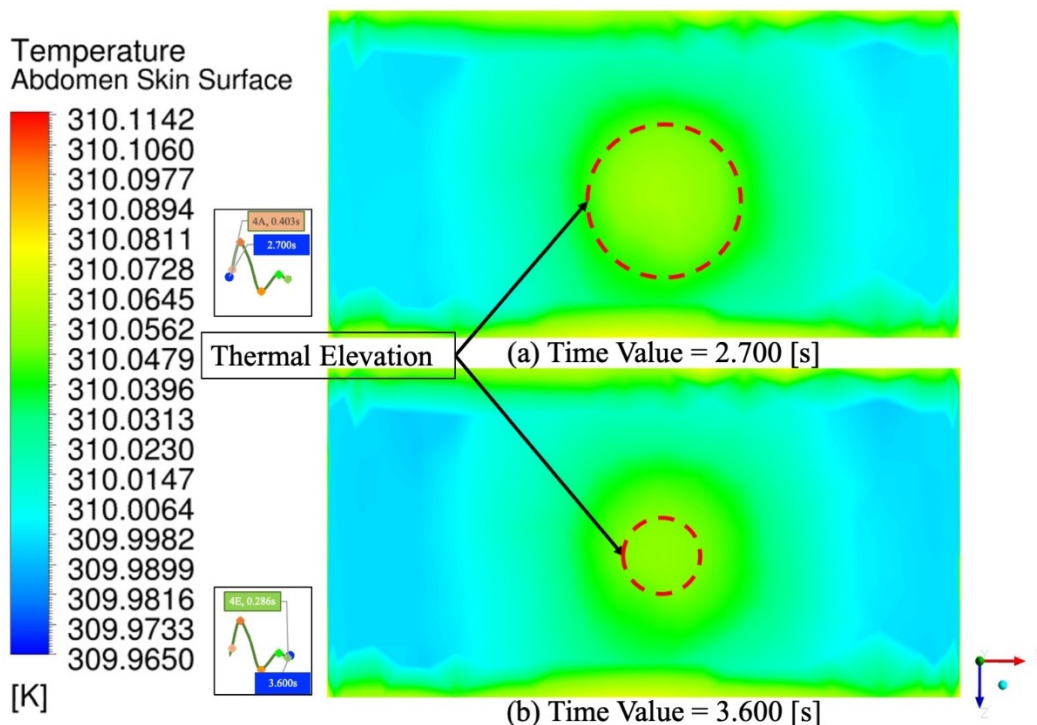

Figure 16. Temperature contours (scaled at min 309.965 K and max 310.115 K) on the midriff skin surface of the AAA midriff skin surface at the (a) start (time stamp = 2.7 s) (b) end (time stamp = 3.6 s) of fourth cardiac cycle of FSI Analysis. A circular thermal elevation over the bulge was observed at the centre of midriff skin surface.

In summary, as illustrated by CFD rigid-wall and FSI Analysis, a positive correlation was found between midriff skin surface isotherms contour and h_c. To elaborate, at lower h_c and supine position on floor, 1) a higher temperature isotherm contour which is closer to blood temperature and 2) a diminishing circular thermal elevation were expected to be observed from thermography.

Taken together, findings highlighted in Section 4.3.2 has shown that CFD rigid-wall Analysis is sufficient to produce decent temperature contour for proof of concept despite it recorded approximately 3 decimal points higher temperature than FSI Analysis.

5. Limitations

One major limitation of this study is the idealised abdomen model. The idealised abdomen model used in this study did not reflect the real case because the thermal effects between other organs, tissues, fat layers were ignored. On the other hand, the abdominal aorta wall was assumed to have a uniform thickness of 0.0015 m by ignoring the presence of intraluminal thrombus (ILT). Therefore, the cumulative effects of wall heterogeneity and material model were omitted [45]. To improve reliability, the patient-specific's abdominal aorta wall properties should be used because the AAA bulge was expected to be less elastic than the proximal and distal neck. In addition, the mechanical properties of both AAA and abdominal tissue were assumed to be isotropic, as supported by numerous FSI studies conducted in the past decades. However, recent FSI studies adopted the real characteristics of AAAs namely, the anisotropic wall material [63]. Chu, Sardar Bilal and Hajizadeh [64] deduced that the heat transfer along walls enhances verses Rayleigh and Darcy parameters whereas delineates against mounting effect of magnetic field parameter. Modelling the AAA wall using anisotropic material had proven to have a more accurate depiction of a more precise behaviour of aorta wall and FSI Analysis, such as peak stress and displacement [17,24]. Lastly, the assumption of supine position on floor made in convection heat transfer regression equation was acceptable for proof of concept in this study.

6. Conclusions

The present study was designed to determine the correlation between CTP and the presence of AAA; temperature (isotherm) contour of midriff skin surface during clinical thermography where the patient was at the supine position at a clinical environment.

One of the most significant findings from this study was that in CFD rigid-wall Analysis, AAA demonstrated CTP in systolic phase only. The systolic phase resulted in a drop of temperature of abdominal aorta wall. However, during the diastolic phase, there was an increase of temperature on the AAA wall. More importantly, the CTP was not observed in FSI Analysis. As such, AAA did not have the CTP as shown in healthy aorta. The absence of CTP could be a good indicator of the presence of AAA. In addition, the outcomes from CFD and FSI analyses show that the thermal physics behaviours of AAA should be studied with more realistic boundary conditions using FSI.

Another second major finding is that when a lower natural convective heat transfer coefficient was applied at the abdomen skin surface, a diminishing circular thermal elevation with higher overall temperature was observed. In comparison to the effect of diastolic phase on AAA wall, there was a higher reduction on the midriff skin temperature. The Pennes' bioheat transfer effect was also more dominant, thereby contributing to a quasi-linear reduction of temperature on the midriff skin surface. Such is indicative that the CTP was not observed at the midriff skin surface of healthy or aneurysm abdominal aortic at all analysis.

Thirdly, the findings from this research on temperature contour of midriff skin surface of AAA provide insights to model as an indirect measure of AAA. A distinct circular thermal signature was

observed through numerical study and it closely resembled experimental study in by Ng and Pang [14]. Notably, from the temperature contour, CFD rigid-wall Analysis may be adequate to predict the thermal signature of midriff skin surface despite a more localised hot-spot was found in FSI Analysis.

Taken together, the highly sensitive IRT method proposed was a potential clinical diagnostic method for AAA as the circular thermal elevation signature on midriff skin surface, was identifiable on a thermal image in a clinical setting. In comparison to the commonly AAA screening procedures such as DUS, CTA and MRA, IRT is a less invasive and more feasible (economical) clinical thermography approach. The results of this study may serve as a reference to detect AAA in various scenarios or natural convective heat transfer coefficient. In addition, clinical trials on AAA patient are called to be conducted to further improve the reliability of the conclusions of this study.

7. Future works

Moving forward, the FSI Analysis could be extended to model a more realistic model by using more lifelike properties for abdominal and AAA model. Firstly, the thermal effects between other organs, tissues, fat layers should be included in the abdomen model to mitigate the limitation of idealised abdomen model discussed in Section 5. Moreover, the cumulative effects of aorta wall heterogeneity and material model could be taken into consideration by including the presence of ILT (if any) and the anisotropic wall property. Other than that, the deformation of midriff skin surface could be studied and analysed for a potential indicator of AAA. To explain, as the abdominal aortic is expanded, the bulge should be taken up more volume within the abdomen cavity, as such, there is a possibility that the bulge would result in an outwards deformation onto the midriff organs and tissue.

Acknowledgments

Conflict of interest

The authors declare that they have no known competing financial interests or personal relationships that could have appeared to influence the work reported in this paper.

References

1. F. A. Lederle, J. A. Freischlag, T. C. Kyriakides, F. T. Padberg, J. S. Matsumura, T. R. Kohler, et al., Outcomes following endovascular vs open repair of abdominal aortic aneurysm: A randomized trial, *JAMA*, **302** (2009), 1535–1542. https://doi.org/10.1001/jama.2009.1426

2. A. Chervu, G. P. Clagett, R. J. Valentine, S. I. Myers, P. J. Rossi, Role of physical examination in detection of abdominal aortic aneurysms, *Surgery*, **117** (1995), 454–457. https://doi.org/10.1016/S0039-6060(05)80067-4

3. B. Keisler, C. Carter, Abdominal aortic aneurysm, *Am. Fam. Phys.*, **91** (2015), 538–543.

4. P. M. Shaw, J. Loree, R. C. Gibbons, *Abdominal Aortic Aneurysm*, StatPearls Publishing, Treasure Island (FL), 2022.

5. T. Canchi, A. Saxena, E. Y. K. Ng, E. C. H. Pwee, S. Narayanan, Application of fluid-structure interaction methods to estimate the mechanics of rupture in asian abdominal aortic aneurysms, *Bionanoscience*, **8** (2018), 1035–1044. https://doi.org/10.1007/s12668-018-0554-z

6. L. Smith-Burgess, Early identification and detection of abdominal aortic aneurysms, *Nurs. Times*, **113** (2017), 36–39.

7. D. C. Brewster, J. L. Cronenwett, J. W. Hallett, K. W. Johnston, W. C. Krupski, J. S. Matsumura, Guidelines for the treatment of abdominal aortic aneurysms: Report of a subcommittee of the Joint Council of the American Association for Vascular Surgery and Society for Vascular Surgery, *J. Vasc. Surg.*, **37** (2003), 1106–1117. https://doi.org/10.1067/mva.2003.363

8. K. C. Kent, R. M. Zwolak, N. N. Egorova, T. S. Riles, A. Manganaro, A. J. Moskowitz, et al., Analysis of risk factors for abdominal aortic aneurysm in a cohort of more than 3 million individuals, *J. Vasc. Surg.*, **52** (2010), 539–548. https://doi.org/10.1016/j.jvs.2010.05.090

9. H. Bengtsson, D. Bergqvist, N. H. Sternby, Increasing prevalence of abdominal aortic aneurysms: A necropsy study, *Eur. J. Surg.*, **158** (1992), 19–23.

10. F. L. Moll, J. T. Powell, G. Fraedrich, F. Verzini, S. Haulon, M. Waltham, et al., Management of abdominal aortic aneurysms clinical practice guidelines of the European society for vascular surgery, *Eur. J. Vasc. Endovasc. Surg.*, **41** (2011), S1–S58. https://doi.org/10.1016/j.ejvs.2010.09.011

11. J. Lieberg, L. L. Pruks, M. Kals, K. Paapstel, A. Aavik, J. Kals, Mortality after elective and ruptured abdominal aortic aneurysm surgical repair: 12-year single-center experience of Estonia, *Scand. J. Surg.*, **107** (2018), 152–157. https://doi.org/10.1177/1457496917738923

12. R. E. Brightwell, A. M. Choong, A. G. Barnett, P. J. Walker, Changes in temperature affect the risk of abdominal aortic aneurysm rupture, *ANZ J. Surg.*, **84** (2014), 871–876. https://doi.org/10.1111/ans.12446

13. A. Saxena, E. Y. K. Ng, C. Manchanda, T. Canchi, Cardiac thermal pulse at the neck-skin surface as a measure of stenosis in the carotid artery, *Therm. Sci. Eng. Prog.*, **19** (2020), 100603. https://doi.org/10.1016/j.tsep.2020.100603

14. E. Y. K. Ng, E. Y. L. Pang, Thermal elevation on midriff skin surface as a potential diagnostic feature for abdominal aortic aneurysm using infrared thermography (IRT), *Int. J. Therm. Sci.*, **172** (2022), 107305. https://doi.org/10.1016/j.ijthermalsci.2021.107305

15. C. M. Scotti, A. D. Shkolnik, S. C. Muluk, E. A. Finol, Fluid-structure interaction in abdominal aortic aneurysms: Effects of asymmetry and wall thickness, *Biomed. Eng. Online*, **4** (2005), 64. https://doi.org/10.1186/1475-925x-4-64

16. W. Hao, S. Gong, S. Wu, J. Xu, M. Go, A. Friedman, et al., A mathematical model of aortic aneurysm formation, *PLoS One*, **12** (2017), e0170807. https://doi.org/10.1371/journal.pone.0170807

17. S. Lin, X. Han, Y. Bi, S. Ju, L. Gu, Fluid-structure interaction in abdominal aortic aneurysm: Effect of modeling techniques, *Biomed Res. Int.*, **2017** (2017), 7023078. https://doi.org/10.1155/2017/7023078

18. G. A. Holzapfel, T. C. Gasser, R. W. Ogden, A new constitutive framework for arterial wall mechanics and a comparative study of material models, *J. Elast.*, **61** (2000), 1–48. https://doi.org/10.1023/A:1010835316564

19. J. Humphrey, Introduction, *World Dev.*, **23** (1995), 1–7. https://doi.org/10.1016/0305-750X(95)90011-O

20. G. A. Holzapfel, R. W. Ogden, Constitutive modelling of arteries, *Proc. Math. Phys. Eng. Sci.*, **466** (2010), 1551–1597. https://doi.org/10.1098/rspa.2010.0058

21. C. Reeps, M. Gee, A. Maier, M. Gurdan, H. H. Eckstein, W. A. Wall, The impact of model assumptions on results of computational mechanics in abdominal aortic aneurysm, *J. Vasc. Surg.*, **51** (2010), 679–688. https://doi.org/10.1016/j.jvs.2009.10.048

22. C. M. Scotti, J. Jimenez, S. C. Muluk, E. A. Finol, Wall stress and flow dynamics in abdominal aortic aneurysms: finite element analysis vs. fluid-structure interaction, *Comput. Methods Biomech. Biomed. Eng.*, **11** (2008), 301–322. https://doi.org/10.1080/10255840701827412

23. J. H. Leung, A. R. Wright, N. Cheshire, J. Crane, S. A. Thom, A. D. Hughes, et al., Fluid structure interaction of patient specific abdominal aortic aneurysms: A comparison with solid stress models, *Biomed. Eng. Online*, **5** (2006), 33. https://doi.org/10.1186/1475-925X-5-33

24. Y. Mesri, H. Niazmand, A. Deyranlou, Numerical study on fluid-structure interaction in a patient-specific abdominal aortic aneurysm for evaluating wall heterogeneity and material model effects on its rupture, *J. Appl. Fluid Mech.*, **10** (2017), 1699–1709. https://doi.org/10.18869/acadpub.jafm.73.243.27678

25. A. Grytsan, P. N. Watton, G. A. Holzapfel, A thick-walled fluid-solid-growth model of abdominal aortic aneurysm evolution: application to a patient-specific geometry, *J. Biomech. Eng.*, **137** (2015). https://doi.org/10.1115/1.4029279

26. H. Schmid, A. Grytsan, E. Poshtan, P. N. Watton, M. Itskov, Influence of differing material properties in media and adventitia on arterial adaptation—Application to aneurysm formation and rupture, *Comput. Methods Biomech. Biomed. Eng.*, **16** (2013), 33–53. https://doi.org/10.1080/10255842.2011.603309

27. K. Y. Volokh, Modeling failure of soft anisotropic materials with application to arteries, *J. Mech. Behav. Biomed. Mater.*, **4** (2011), 1582–1594. https://doi.org/10.1016/j.jmbbm.2011.01.002

28. P. N. Watton, N. A. Hill, M. Heil, A mathematical model for the growth of the abdominal aortic aneurysm, *Biomech. Model. Mechanobiol.*, **3** (2004), 98–113. https://doi.org/10.1007/s10237-004-0052-9

29. M. L. Raghavan, D. A. Vorp, Toward a biomechanical tool to evaluate rupture potential of abdominal aortic aneurysm: identification of a finite strain constitutive model and evaluation of its applicability, *J. Biomech.*, **33** (2000), 475–482. https://doi.org/10.1016/S0021-9290(99)00201-8

30. M. J. Riedl, *Optical Design Fundamentals for Infrared Systems*, SPIE press, Bellingham, 2001.

31. A. Saxena, E. Y. K. Ng, M. Mathur, C. Manchanda, N. A. Jajal, Effect of carotid artery stenosis on neck skin tissue heat transfer, *Int. J. Therm. Sci.*, **145** (2019), 106010. https://doi.org/10.1016/j.ijthermalsci.2019.106010

32. G. Varjú, C. F. Pieper, J. B. Renner, V. B. Kraus, Assessment of hand osteoarthritis: Correlation between thermographic and radiographic methods, *Rheumatology*, **43** (2004), 915–919. https://doi.org/10.1093/rheumatology/keh204

33. K. Woźniak, L. Szyszka-Sommerfeld, G. Trybek, D. Piątkowska, Assessment of the sensitivity, specificity, and accuracy of thermography in identifying patients with TMD, *Med. Sci. Monit.*, **21** (2015), 1485–1493. https://doi.org/10.12659/MSM.893863

34. S. V. Patankar, *Numerical Heat Transfer and Fluid Flow*, CRC Press, Boca Raton, (1980), 214.

35. C. Childs, H. Soltani, Abdominal cutaneous thermography and perfusion mapping after caesarean section: A scoping review, *Int. J. Environ. Res. Public Health*, **17** (2020), 8693. https://doi.org/10.3390/ijerph17228693

36. R. B. Barnes, Thermography of the human body, *Science*, **140** (1963), 870–877. https://doi.org/10.1126/science.140.3569.870

37. O. Ley, T. Kim, Determination of atherosclerotic plaque temperature in large arteries, *Int. J. Therm. Sci.*, **47** (2008), 147–156. https://doi.org/10.1016/j.ijthermalsci.2007.01.034

38. T. Canchi, S. D. Kumar, E. Y. K. Ng, S. Narayanan, A review of computational methods to predict the risk of rupture of abdominal aortic aneurysms, *Biomed. Res. Int.*, **2015** (2015), 861627. https://doi.org/10.1155/2015/861627

39. J. Xu, A. Psikuta, J. Li, S. Annaheim, R. M. Rossi, Influence of human body geometry, posture and the surrounding environment on body heat loss based on a validated numerical model, *Build. Environ.*, **166** (2019), 106340. https://doi.org/10.1016/j.buildenv.2019.106340

40. Y. Kurazumi, T. Tsuchikawa, N. Matsubara, T. Horikoshi, Convective heat transfer area of the human body, *Eur. J. Appl. Physiol.*, **93** (2004), 273–285. https://doi.org/10.1007/s00421-004-1207-1

41. Y. Kurazumi, T. Tsuchikawa, J. Ishii, K. Fukagawa, Y. Yamato, N. Matsubara, Radiative and convective heat transfer coefficients of the human body in natural convection, *Build. Environ.*, **43** (2008), 2142–2153. https://doi.org/10.1016/j.buildenv.2007.12.012

42. K. Ouriel, R. M. Green, C. Donayre, C. K. Shortell, J. Elliott, J. A. DeWeese, An evaluation of new methods of expressing aortic aneurysm size: Relationship to rupture, *J. Vasc. Surg.*, **15** (1992), 12–20. https://doi.org/10.1016/0741-5214(92)70008-9

43. C. M. Scotti, E. A. Finol, Compliant biomechanics of abdominal aortic aneurysms: A fluid-structure interaction study, *Comput. Struct.*, **85** (2007), 1097–1113. https://doi.org/10.1016/j.compstruc.2006.08.041

44. S. Bernad, E. Bernad, T. Barbat, C. Brisan, V. Albulescu, An analysis of blood flow dynamics in AAA, in *Etiology, Pathogenesis and Pathophysiology of Aortic Aneurysms and Aneurysm Rupture*, IntechOpen, 2011.

45. W. S. Cobb, J. M. Burns, K. W. Kercher, B. D. Matthews, H. J. Norton, B. T. Heniford, Normal intraabdominal pressure in healthy adults, *J. Surg. Res.*, **129** (2005), 231–235. https://doi.org/10.1016/j.jss.2005.06.015

46. B. Hernández-Gascón, E. Peña, H. Melero, G. Pascual, M. Doblaré, M. P. Ginebra, et al., Mechanical behaviour of synthetic surgical meshes: Finite element simulation of the herniated abdominal wall, *Acta Biomater.*, **7** (2011), 3905–3913. https://doi.org/10.1016/j.actbio.2011.06.033

47. E. S. Di Martino, G. Guadagni, A. Fumero, G. Ballerini, R. Spirito, P. Biglioli, et al., Fluid-structure interaction within realistic three-dimensional models of the aneurysmatic aorta as a guidance to assess the risk of rupture of the aneurysm, *Med. Eng. Phys.*, **23** (2001), 647–655. https://doi.org/10.1016/S1350-4533(01)00093-5

48. M. H. Cardoso, Experimental study of the human anterolateral abdominal wall: Biomechanical properties of fascia and muscles, 2012. Available from: https://repositorio-aberto.up.pt/bitstream/10216/65576/1/000154315.pdf.

49. *ANSYS Mechanical Material Reference*, Release 2021 R1 ed., ANSYS, Inc., Canonsburg, (2021), 93–106.

50. J. Xiang, V. M. Tutino, K. V. Snyder, H. Meng, CFD: Computational fluid dynamics or confounding factor dissemination? The role of hemodynamics in intracranial aneurysm rupture risk assessment, *Am. J. Neuroradiol.*, **35** (2014), 1849–1857. https://doi.org/10.3174/ajnr.A3710

51. F. Gijsen, F. van de Vosse, J. D. Janssen, The influence of the non-Newtonian properties of blood on the flow in large arteries: Steady flow in a carotid bifurcation model, *J. Biomech.*, **32** (1999), 601–608. https://doi.org/10.1016/S0021-9290(99)00015-9

52. K. Perktold, M. Resch, H. Florian, Pulsatile non-Newtonian flow characteristics in a three-dimensional human carotid bifurcation model, *J. Biomech. Eng.*, **113** (1991), 464–475. https://doi.org/10.1115/1.2895428

53. J. P. V. Geest, M. S. Sacks, D. A. Vorp, The effects of aneurysm on the biaxial mechanical behavior of human abdominal aorta, *J. Biomech.*, **39** (2006), 1324–1334. https://doi.org/10.1016/j.jbiomech.2005.03.003

54. D. A. Vorp, M. L. Raghavan, M. W. Webster, Mechanical wall stress in abdominal aortic aneurysm: Influence of diameter and asymmetry, *J. Vasc. Surg.*, **27** (1998), 632–639. https://doi.org/10.1016/S0741-5214(98)70227-7

55. S. Pasta, A. Rinaudo, A. Luca, M. Pilato, C. Scardulla, T. G. Gleason, et al., Difference in hemodynamic and wall stress of ascending thoracic aortic aneurysms with bicuspid and tricuspid aortic valve, *J. Biomech.*, **46** (2013), 1729–1738. https://doi.org/10.1016/j.jbiomech.2013.03.029

56. J. Pearce, S. Thomsen, Blood vessel architectural features and their effects on thermal phenomena in *Matching the Energy Source to the Clinical Need: A Critical Review*, SPIE, (2000), 122–168.

57. F. A. Duck, Chapter 2—Thermal properties of tissue, in *Physical Properties of Tissues* (ed. F. A. Duck), Academic Press, London, (1990), 9–42.

58. G. Giannakoulas, G. Giannoglou, J. Soulis, T. Farmakis, S. Papadopoulou, G. Parcharidis, et al., A computational model to predict aortic wall stresses in patients with systolic arterial hypertension, *Med. Hypotheses*, **65** (2005), 1191–1195. https://doi.org/10.1016/j.mehy.2005.06.017

59. G. J. Müller, A. Roggan, *Laser-induced Interstitial Thermotherapy*, SPIE Optical Engineering Press, 1995.

60. M. Halabian, B. Beigzadeh, A. Karimi, H. A. Shirazi, M. H. Shaali, A combination of experimental and finite element analyses of needle–tissue interaction to compute the stresses and deformations during injection at different angles, *J. Clin. Monit. Comput.*, **30** (2016), 965–975. https://doi.org/10.1007/s10877-015-9801-9

61. S. Mukhopadhyay, M. S. Mandal, S. Mukhopadhyay, Heat transfer in pulsatile blood flow obeying Cross viscosity model through an artery with aneurysm, *J. Eng. Math.*, **131** (2021), 6. https://doi.org/10.1007/s10665-021-10172-w

62. Y. G. Stergiou, A. G. Kanaris, A. A. Mouza, S. V. Paras, Fluid-structure interaction in abdominal aortic aneurysms: Effect of haematocrit, *Fluids*, **4** (2019), 11. https://doi.org/10.3390/fluids4010011

63. J. D. Humphrey, G. A. Holzapfel, Mechanics, mechanobiology, and modeling of human abdominal aorta and aneurysms, *J. Biomech.*, **45** (2012), 805–814. https://doi.org/10.1016/j.jbiomech.2011.11.021

64. Y. Chu, D. S. Bilal, M. Hajizadeh, Hybrid ferrofluid along with MWCNT for augmentation of thermal behavior of fluid during natural convection in a cavity, *Math. Methods Appl. Sci.*, 2020. https://doi.org/10.1002/mma.6937

Appendix

a. Pennes bioheat equation UDF

```
/***************************************************************
UDF for Pennes Bioheat Equation (FSI)
***************************************************************/
#include "udf.h"
DEFINE_SOURCE(tissue, cell, thread, dS, eqn)
{
real source;
real temp = C_T(cell, thread);
real metabolic = 684;
double V_t=0.01178;
source = (1085*3768*0.5380*V_t)*(310.15-temp)+metabolic;
dS[eqn] = 0;
return source;
}
```

b. Inlet pulsatile velocity equation UDF

```
/***************************************************************
UDF for Inlet Pulsatile Velocity UDF (FSI & CFD rigid-wall Analysis)
***************************************************************/
#include "udf.h"
DEFINE_PROFILE(inlet_3D_parabolic,thread,index)
{
real x[3];
real R = 0.013;
face_t f;
real t = CURRENT_TIME;
begin_f_loop(f,thread)
{
F_CENTROID(x,f,thread);
F_PROFILE(f,thread,index)  =  (0.3899  +  0.1155*cos(6.981*t)  +  0.1962*sin(6.981*t)  -
0.141*cos(2*6.981*t) + 0.03545*sin(2*6.981*t) - 0.02596*cos(3*6.981*t) + 0.006594*sin(3*6.981*t)
-  0.02411*cos(4*6.981*t)  -  0.001696*sin(4*6.981*t)  +  0.0008816*cos(5*6.981*t)  -
0.01011*sin(5*6.981*t))*(1-(x[1]*x[1]+x[0]*x[0])/(R*R));
}
end_f_loop(f,thread)
}
```

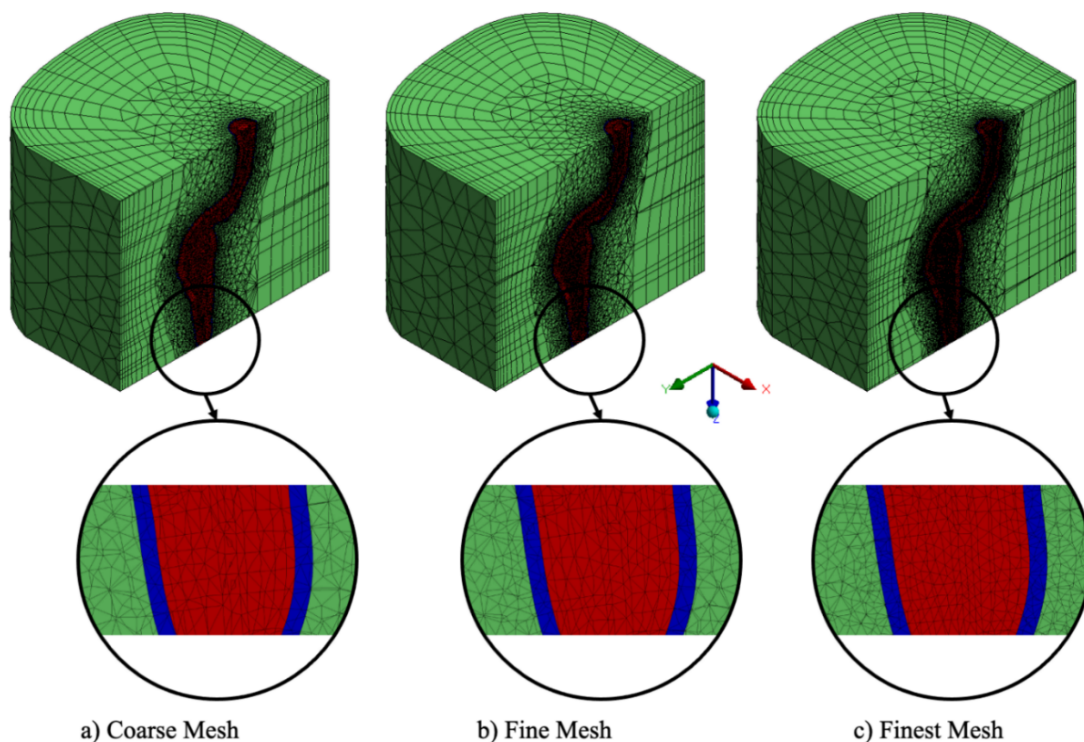### c. Mesh convergence study—Mesh size setups

a) Coarse Mesh   b) Fine Mesh   c) Finest Mesh

Figure A1. Various mesh setups in mesh convergence study. To be used in conjunction with Table 5.
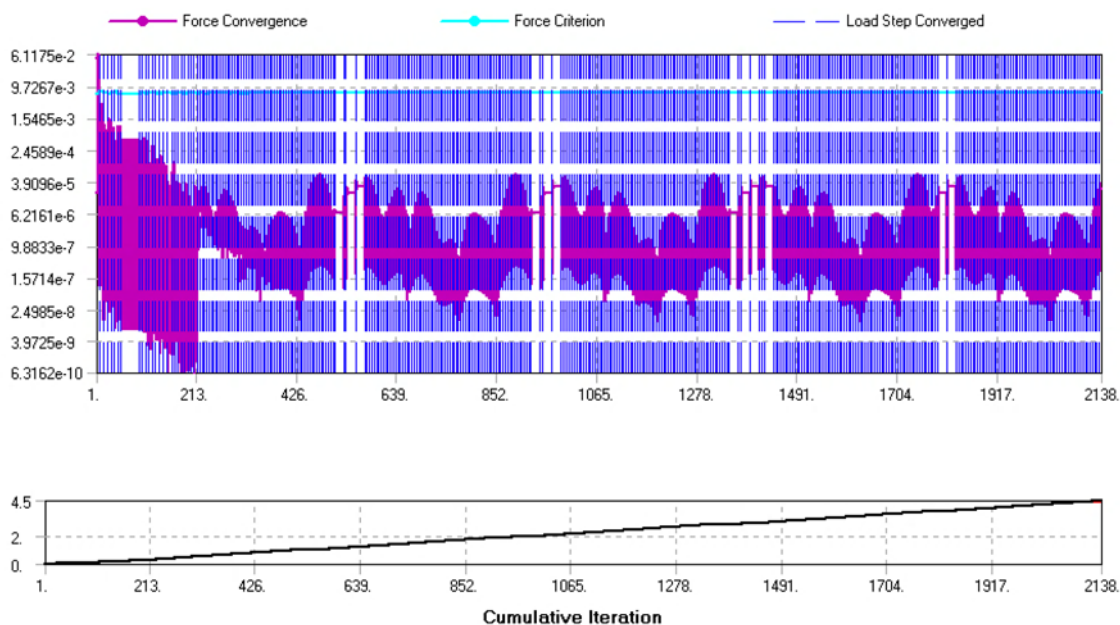
d. Convergence criteria

d.i. FEA solver

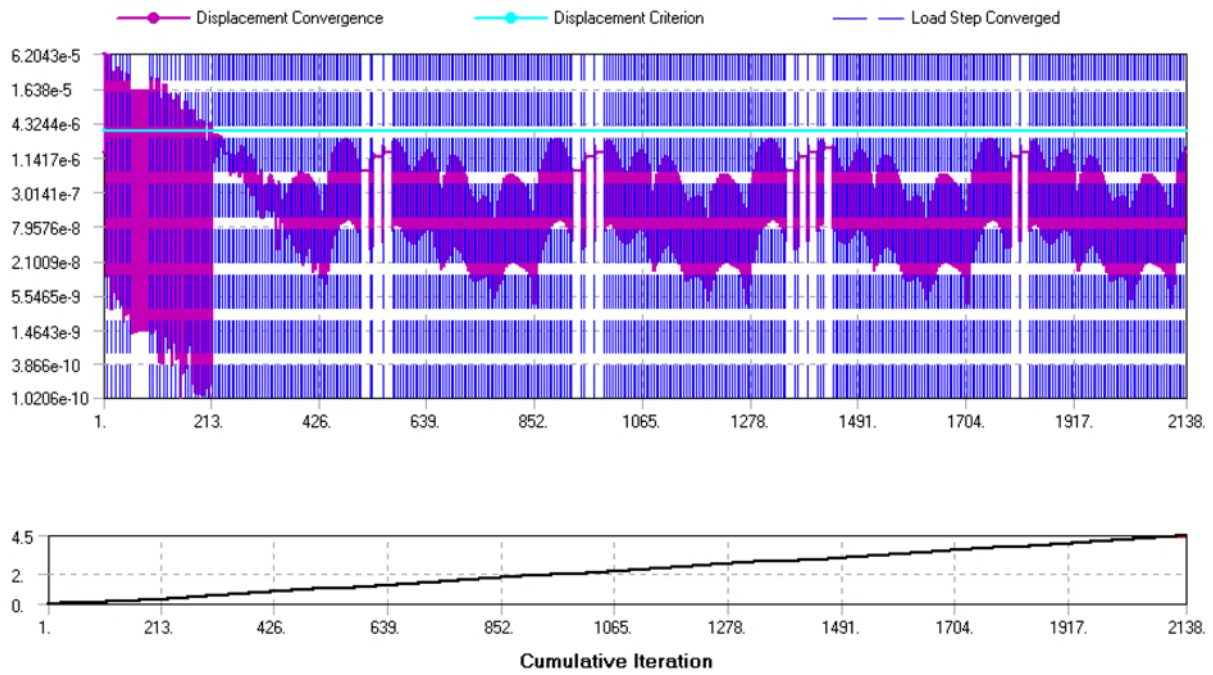**Figure A2.** Force convergence graph on FEA solver.

Figure A3. Displacement convergence graph on FEA solver.
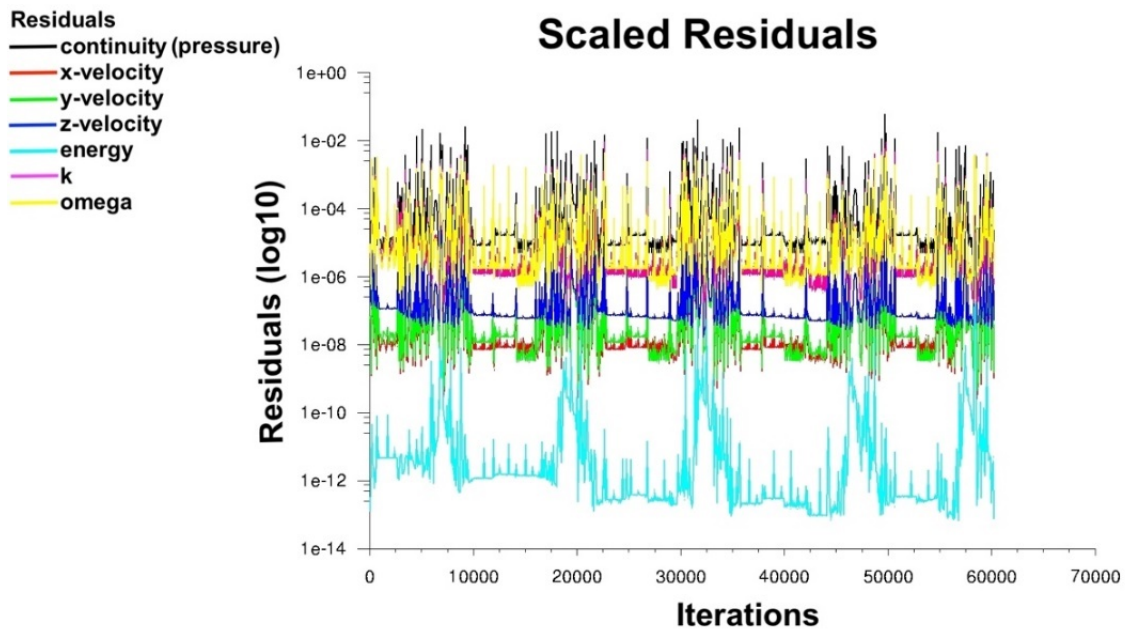
d.ii. CFD solver

Figure A4. Residual plot for transient FSI Analysis.
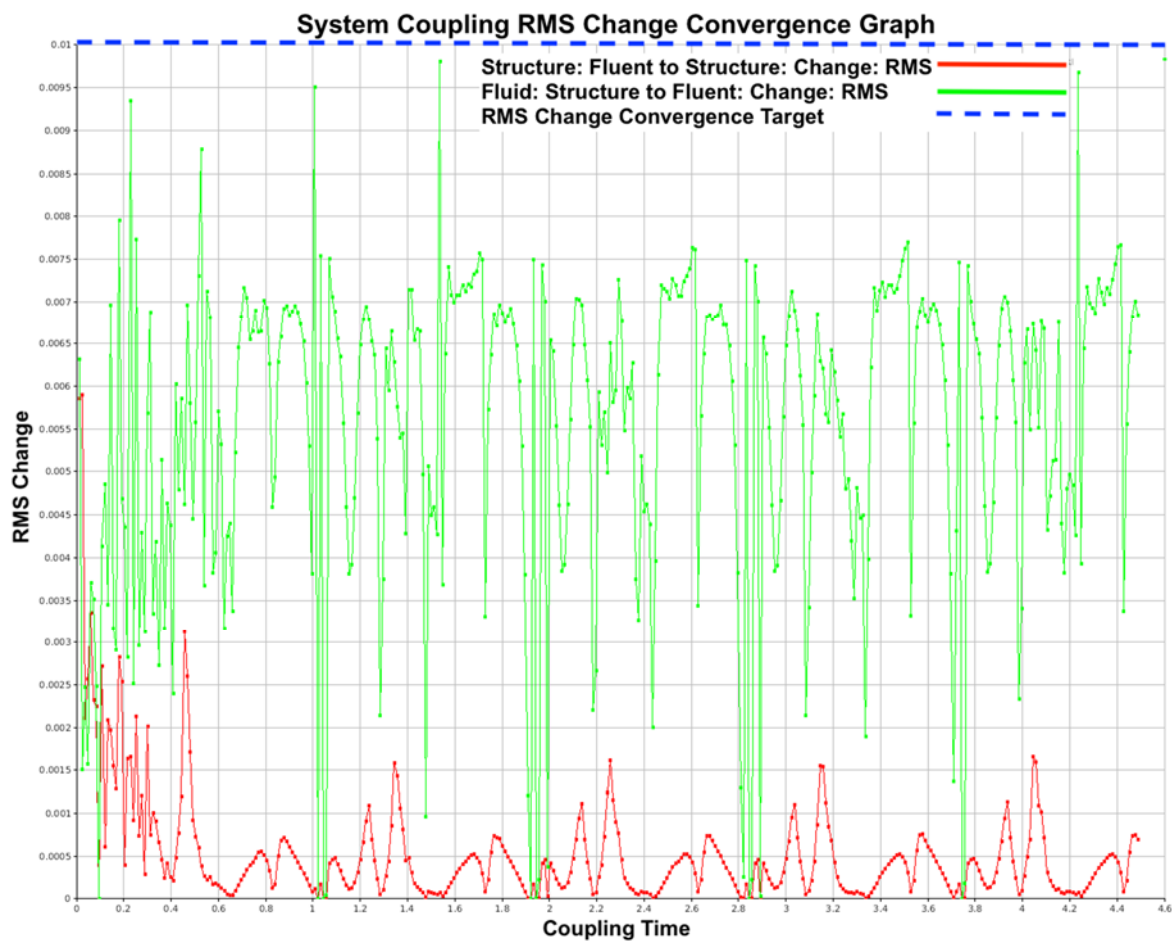
d.iii. System coupling

Figure A5. System coupling RMS change convergence graph.